IMPACT OF SURFACE HYDROXYLATION ON STABILITY OF SILICA-SUPPORT METAL NANOPARTICLES: ON THE WAY TO TAILOR THE CATALYSTS

by

Wanling Zhu

Bachelor of Science in Pharmaceutical Engineering,

East China University of Science and Technology, 2015

Submitted to the Graduate Faculty of

Swanson School of Engineering in partial fulfillment

of the requirements for the degree of

Master of Science

University of Pittsburgh

2017

UNIVERSITY OF PITTSBURGH

SWANSON SCHOOL OF ENGINEERING

This thesis was presented

by

Wanling Zhu

It was defended on

May 30, 2017

and approved by

James R. McKone, Ph.D., Assistant Professor,

Department of Chemical and Petroleum Engineering

Tevis Jacobs, Ph.D., Assistant Professor,

Department of Mechanical Engineering and Materials Science

Thesis Advisor:

Götz Veser, Ph.D., Professor,

Department of Chemical and Petroleum Engineering

IMPACT OF SURFACE HYDROXYLATION ON STABILITY OF SILICA-SUPPORT METAL NANOPARTICLES: ON THE WAY TO TAILOR THE CATALYSTS

Wanling Zhu, M.S.

University of Pittsburgh, 2017

Catalysts lie in the central role in chemical reactions and act as the heart of countless chemical protocols, from academic research at laboratories scale to the chemical industry level. Nanocatalysts are the catalysts composed of nanoparticles, usually have some active metal nanoparticles sit on some types of the supports. Metal nanoparticles (NPs) are characterized by a very high surface area to volume ratio and a large number of low coordination sites. These properties make them highly desired act as active components in catalytic reactions and other applications. However, this high number of low coordination sites also strongly destabilizes particles and makes them prone to sintering then leads to the loss of active surface area, reaction activity and selectivity.

Recently, computational simulations from our group developed the amorphous silica model as the support in platinum-silica catalyst system using a combination of classical molecular modeling and density functional theory (DFT) calculations. In those studies, nanoparticle adhesion energetics and charge transfer were both found to be depend on the silica surface hydroxyl density. Since the hydroxylation is easily tunable by pretreatment temperature,

this suggest that both electronic charge and catalyst stability can be modified via catalyst calcination.

In this work, the platinum NPs dispersed on amorphous silica support were used as model catalysts. Two silica supports with different hydroxyl densities were investigated to explore the impact of surface hydroxylation on stability and reactivity of the catalysts.

Through particle size analysis obtained by X-ray diffraction (XRD) and transmission electron microscopy (TEM) after elevated temperature treatment, we found that Pt NPs on fully hydroxylized silica is more stable than on dehydroxylized silica, with NPs on the former growing to only around half the size compared to those on dehydroxylized catalysts at 800 ºC.

Finally, we analyzed the reactivity of these two catalysts in CO oxidation and found that the ignition temperature of dehydroxylized catalysts was about 30 ºC higher than that of the rehydroxylized catalysts, which correlates well with improved thermal stability of this catalyst.

Overall, our results confirm that the degree of surface hydroxylation of silica has strong impact on both stability and reactivity of the silica-supported metal nanocatalysts.

TABLE OF CONTENTS

LIST OF TABLES

LIST OF FIGURES

PREFACE

Two years ago, I started this research as a catalysis project, but it turned out to be a long battle against a small particle. This thesis expresses the long days spent in the lab, battling shoulder to shoulder with my fellows and friends, the joy for the synthesis, the hope for expected results and the sadness and tiredness with each failed attempt.

I would like to be extremely appreciated to all the people who care and help me with this work. I'm grateful for the patient guidance and supports from my advisor. Dr. Götz Veser always helped me to think critical about any results I got, and continually pushed me to stay focus on the big picture of the project.

I would also like to thank all the lab fellows that help me with my thesis. Especially thank Yahui Yang for teaching me all the techniques in lab, lots of advice of my work and excellent characterization of my samples. And I want to thank Yu-Chieh Cheng for sharing experiment advice and cooperating with me in the project.

Finally, I would like to express my great thanks to my family thousands of miles away, who provide infinite supports of my life and total understanding for my study abroad. Without these courage, I won't make this work a success.

1.0 INTRODUCTION

1.1 CATALYSTS

Catalysts play a central role in chemical reactions and act as the heart of countless chemical protocols, from academic research at laboratories scale to the chemical industry level.[1] They are crucial in the processing of foods, medicines and agriculture industry, the refining of crude oil, the manufacture of plastics, fertilizers, and the production of many different main chemicals in engineering.[2–4] According to Global Catalyst Market,[5] global demand on catalysts was valued at $33.5 billion in 2014 and will witness robust growth in following years. By using a catalyst, which accelerates a chemical reaction without being consumed itself in the process, one can reduce the activation energy of the transformation (illustrates in Figure 1), minimize reagent waste and enhance the selectivity of a reaction by avoiding side reactions, thus leading towards "green chemistry". In the absence of catalysts, a huge number of chemical reactions of significant importance would proceed very slowly or even won't happen, although the reaction conditions such as system temperature and pressure, are thermodynamically favorable for the occurrence of the reactions.

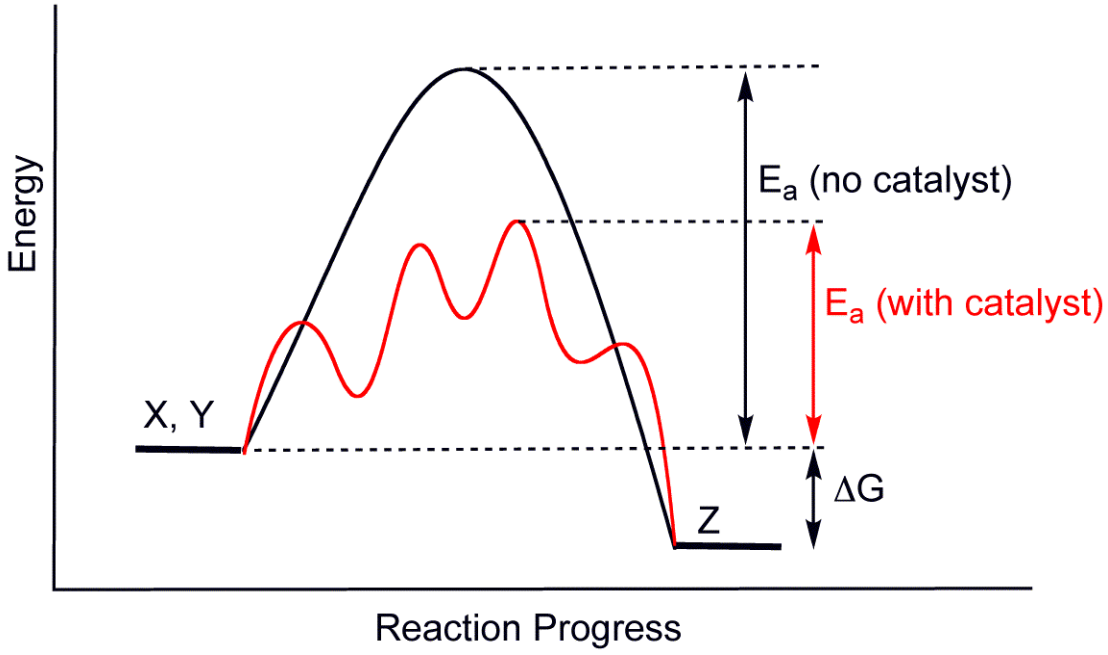

Figure 1 Generic potential energy diagram showing the effect of a catalyst in a hypothetical exothermic chemical reaction X + Y to give Z. The presence of the catalyst opens a different reaction pathway (shown in red) with a lower activation energy. The result and the overall thermodynamics are the same. Schematic cited from Wikipedia. [6]

Nanocatalysts are catalysts containing nanoparticles (particle diameter between 1 to 100 nanometers or 10^{-9} ~ 10^{-7} meters), typically composed of active metal nanoparticles on various supports. Because of the size of catalysts is in nano-scale, which results in surface areas several orders higher than those of conventional catalysts, combined with high reactivity of some transition metal nanoparticles, the reactivity of catalysts raises dramatically. Furthermore, nanocatalysts can still be cost-efficient even utilizing noble metal particles due to the very high utilization of the metal (due to the large surface-to-volume ratio). In view of these abundant advantages of nanocatalysts, they have the potential to replace conventional catalysts (non-nano)

in many applications. However, despite decades of in-depth study, the interactions on the atomic level of nanocatalysts are still not fully understood. Thus, how the physical properties of nanoparticles affect their catalytic properties, and how synthesis parameters can in turn tune those physical properties are key questions waiting to be answered. By better understanding these, nanocatalysts can be designed and engineered to reach the customized physical and chemical properties in industry.

Nanocatalysts can be synthesized by many different methods such as thermal decomposition, sol-gel technique, chemical precipitation, photochemical method, hydrothermal method, wet-chemical method, microwave irradiation, and ultrasonic method.[7–10] The physical properties of nanocatalysts can vary significantly for different types of methods.[11–16]

The discovery and development of catalysts can be shown as the hierarchical workflow in Figure 2. It illustrates three distinct phases of research leading to fully developed catalysts. In this work, we mainly focus concentration on the tertiary screen variable: stability of the catalysts, which is a very basic, fundamental but critical and necessary property of the catalysts for both academic research and industrial practice.

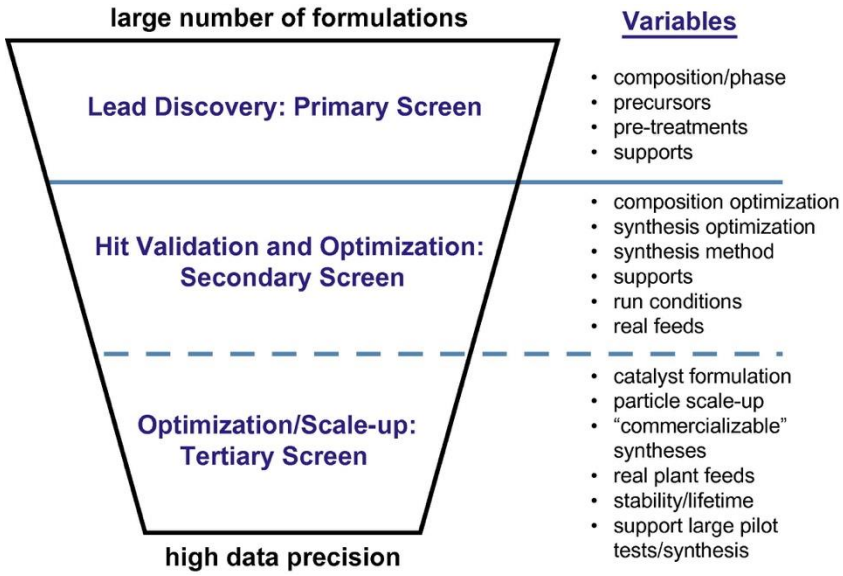

Figure 2 Stages of catalysts discovery and optimization showing variables generally screened in each stage. Generated by Howard and etc. [117]

1.2 METAL NANOPARTICLES

Metal nanoparticles (MNPs) are characterized by a very high surface area to volume ratio, a large number of low coordination sites, and unique electronic properties between the molecular and metallic states.[17] These features make them desirable as active components in catalytic reactions and other applications.[18–21] Besides, their surface properties can be easily tuned via the stabilizers or using a support. In practical studies, the properties of MNPs such as chirality, reactivity could be influenced or transferred by capping agents (polymers, ionic liquids, surfactants etc.) used in the synthesis process and these properties could also depend on the supports, for example, alumina, silica, carbon, ceria etc. With intensive investigations and highly development of the synthesis methods, the MNPs, especially the transition metals become the key role in both homogenous and heterogeneous catalysts. However, the high proportion of

surface atoms that offer plenty of active sites also strongly destabilizes particles and makes them prone to sintering, then leads to the loss of active surface area, reaction activity and selectivity. [22] Together with diminishing supplies of precious metals, increasing demand of market and recovery or recyclability from an industrial view, it makes finding practical solutions to rational design the catalysts with high resistant to sintering dramatically urgent.

Recently, a crucial element in rapid development of metal NPs applications is related with the well-defined synthesis of MNPs. The concept of bottom-up approach for well-controlled NPs in shape, size, surface chemistry and compositions etc. was produced.[23–25] Instead of starting with large materials, this method allows to begin from atoms and molecules, then get rearranged and assembled to larger nanostructures.[26,27] It requires well-understanding of the short-range forces of attraction, e.g. Van der Waals forces, electrostatic forces, and different types of intermolecular forces. MNPs with small size (1~6 nm) and narrow particle size distribution draw a huge attention of scientific interests since they can be used in understanding the quantum size effect and provide new opportunities for optical and electrical materials. They act high reactivity and selectivity in various organic reactions, like the hydrogeneration, hydration, and visible light hydrogen evolution. In previous studies, capping agents as protection such as polymers, ionic liquids, surfactants and organic ligands are widely used to obtain stable metal NPs with small size. However, the MNPs with these capping agents need further purification such as calcination at high temperature to remove the protective compounds. But these thermal treatments would affect the surface properties (e.g. hydroxyl density) of the supports. Additionally, the capping agents also prevent the MNPs directly bond with the supports. Therefore, a novel method to synthesis “unprotected” MNPs needs to be applied when study the metal-support interactions. Curtis and co-workers developed an “unprotected” copper NPs in methanol successfully by the

reduction reaction of copper salts with hydrazine hydrate.[28] Klabunde [29] and Esumi [30] both prepared Pd NPs colloids in organic solvents (acetone, propanol or methyl isobutyl ketone) in the range of 6 to 10 nm and could use for further metal film production. Wang *et al.*[31] reported a simple synthesis method to produce 1~3 nm Pt NPs colloids in ethylene glycol. They also found that the method can transfer to synthesize small particle size of Rh and Ru NPs. The prepared NPs could remain small size for several months and can be separated as solids from solution then further modified by different capping agents to form "protected" NPs. These "unprotected" synthesis methods devote to preparing new functional materials containing corresponding metal NPs.

1.3 AMORPHOUS SILICON DIOXIDE

Amorphous silicon dioxide plays a pivotal role in areas such as pharmaceuticals, optics, nanomaterials coatings and biosensors. It also has a wide range of applications as the catalysts support due to many advantages, such as good stability through thermal treatment, and easy to synthesis in both academic and industrial area with tunable size, functional groups and surface area. The silica surface consists of a combination of silanol groups with different type which the relative concentration highly depends on pretreatment temperature, ambient humidity and thermal treatment time.[32]

The term of hydroxyl groups bond with silica atoms to form silanol groups was first established by several researchers. The studies presented by Hofmann, Endell, Wilm, *et al.* shown that the silanol or hydroxyl groups existed on the surface of the silicas and silicates.[33–35] Further on 1936, Kiselev proved that the water collected from the calcination of silica was not

only from the physisorbed water molecules but also from the chemically bond water inside of the silica through the measurement of wetting heat, then compared with adsorption data and chemical analysis data from literatures. And this finding also suggested that the mechanism of dihydroxylation. The first time of direct evidence proving the existence of surface hydroxyl groups on the silica surface was carried by Yaroslavsky and co-workers.[36] They used an infrared spectroscopy to show that the OH groups adsorption peak on the porous glass. As the development of spectral and chemical analysis techniques, numerical works have explicitly confirmed the presence of hydroxyl groups on silica surface.

In general, silanol groups (≡Si-O-H) would be formed in two ways: one is that the groups are generated through the synthesis of amorphous silica, for example, during the condensation polymerization of $Si(OEt)_4$, -OEt would react with hydrogen from water and left –OH group bond with Si atom. Surface hydroxyl groups can be also formed as a result of rehydroxylation of dehydroxylized silica (also refer as silicon) when it is treated directly with water or aqueous solutions. The silica surface acts as the oxide adsorbent and its surface properties depend on the density of the silanol groups. During the adsorption process, the silanol groups present as the center points and could form the hydrogen bonds with the adsorbates through the donor-acceptor mechanism. Thus, the density of the silanol groups highly correlate with the degree of the adsorption, and fully dehydroxylized silica could lead to more hydrophobic properties.[37]

Surface OH groups can be differentiated into several classes and show in Figure 3: isolated or single free silanol groups, ≡Si-O-H; geminal free (geminal silanols or silanediols), $=Si(OH)_2$; vicinal, or OH groups bond through the hydrogen bond; siloxane groups (silica atoms bond with oxygen only), ≡Si-O-Si≡; and internal silanols, or structurally bond water inside the ultramicropores (pores diameter less than 1 nm) of silica skeleton.

Many problems related with the surface of the silica are attracted considerable concentrations. Some previous studies have shown that many materials properties like reactivity and surface hydrophobicity are related with the content of silanol groups.[38]

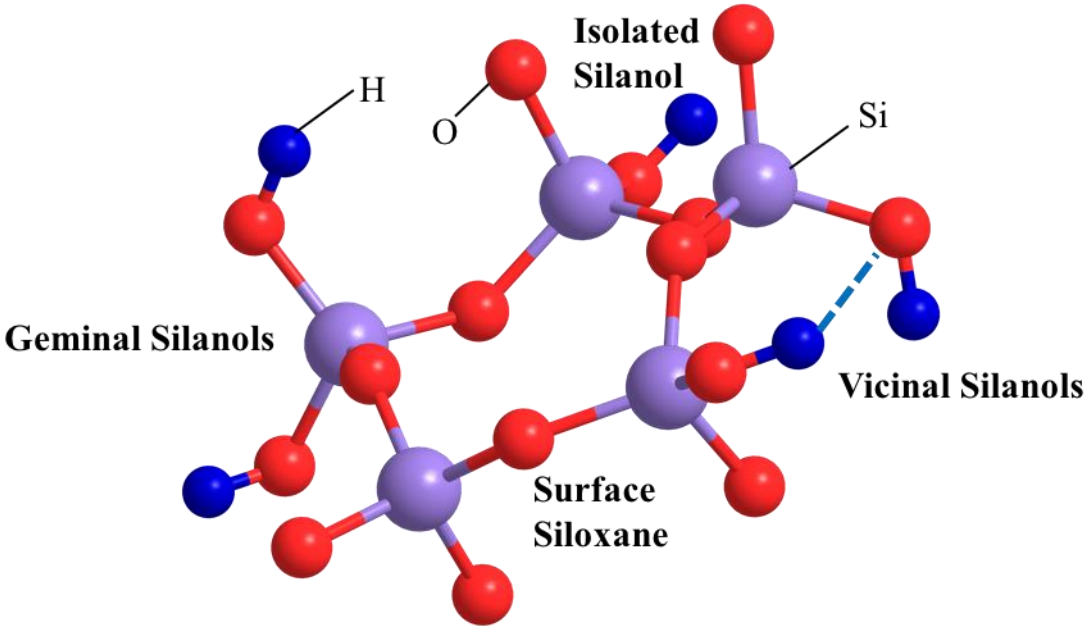

Figure 3 Classification of silanol groups and siloxane bridges on the surface of amorphous silica: surface siloxanes, isolated silanols, geminal silanols and vicinal silanols. 3D plot generated via ChemDraw.

In order to characterize the surface properties of the silica, for example, the concentration and distribution of different types of hydroxyl groups, Zhuravlev [39] made a study of the structure characterization of varies silica sample and established a model to show the determining factor of the surface silanol groups and siloxane bridges. He proposed that the concentration of silanol groups depended on the thermal pretreatment (such as the calcination) of the silica and the

maximum of silanol density would be close to 5 nm^{-2} regardless of various silica with different size and specific surface area.

1.4 METAL-SUPPORTED NANOCATALYSTS

Metal NPs well dispersed on the surface of oxide supports such as silica, alumina, ceria build the most of nanocatalysts with wide applications on sustainable energy, environmental pollution prevention, and biomedical fields. The catalytic activity, selectivity and lifetime of these materials always rely on the detailed structure, particle size and the choice of supports.[40–43]

In most synthesis of catalysts, oxidation or reduction at specific temperatures cannot be avoided for the preparation of high surface area catalysts. However, these thermal treatments may lead to morphological and chemical changes of the metal particles dispersed on the support result from sintering or metal-support interactions. Hence, it is importance to study and define optimal conditions for catalyst preparation, pretreatment and further behavior in actual reaction.[44] There are various changes in morphology caused by the metal-support interaction have been reported vary from different metal-support systems, for example sintering,[45–49] encapsulation,[50,51] inter-diffusion,[52,53] and alloy formation.[54,55]

In particular, silicide formation between metals and SiO_2 in a catalyst has been shown to alter catalytic activity and selectivity.[56,57] For instance, Juszczyk and co-workers had already shown that Pd-silicide structure was observed during the high temperature reduction of Pd/SiO_2, which improves selectivity for the isomerization of neopentane dramatically.[57] However, there are still some unresolved questions and issues on metal-support interactions in supported silica catalysts even though large amount of published studies on silica supports fields. For example,

the understanding of metal-support interactions between metals and SiO_2 on molecular level, effects of hydroxyl groups on silica interact with metal, etc.

Campbell *et al.* shown that the chemical potential of the metal atoms on supported nanoparticles related with the chemical activity of these catalysts. The higher chemical potential led to stronger bond with small adsorbates and rapid sintering deactivation since the metal atoms encountered a larger thermodynamic driving force. Furthermore, they proved that the chemical potential of metal atoms increased with the decrease of particle size and adhesive energy, which also supported the increase of deactivation speed of small particles.[58–60] Recently they reported the adhesive energy between metal atoms with supports could be predicted with the nature of metal and of the support surface through the experimental measurements.[61] In addition, Ewing *et al.* established a model of Pt clusters sit on amorphous silica, and shown that Pt-silica interaction energy and resistance to sintering to be highly related with the number of Pt-silica bonds formed during nanoparticles deposition, and therefore, directly related to the surface property of silica: silanol number.[62] Hence, the aim of this work is to prove the thermal stability of Pt on amorphous silica catalysts relies on the surface hydroxyl density of silica supports through experiments and further to investigate the reactivity differences impacted by thermal stability of silica in different OH density.

2.0 EXPERIMENTS METHODS

2.1 CHEMICAL REAGENTS

Dihydrogen hexachloroplatinate (IV) hydrate (H_2PtCl_6•$6H_2O$, 99.9% metals basis) and tetraethyl orthosilicate ($Si(OEt)_4$, 99.0%) were purchased from Alfa Aesar Co. and Aldrich Co separately. Ethanol (190 proof) was purchased from Decon Labs. Inc. 2-proponal was supplied by Fisher Chemical. Ammonia bicarbonate (NH_4HCO_3, 99.0%), ethylene glycol (99.8%), sodium hydroxide, ammonium hydroxide solution (28.0~30.0% NH_3 basis) cyclohexane (99.0%) and Brij58 (99.0%, average molar weight around 1124) were purchased from Sigma Aldrich Co. All the chemicals were used as received and without further purification.

2.2 MATERIAL SYNTHESIS

2.2.1 Synthesis of Amorphous Silicon Dioxide

First of all, to confirm the computational work from Ewing's [62,63] study, the amorphous silicon dioxide should ideally be a flat surface support compared to the platinum nanoparticles. Hence, a relative large sphere of amorphous silicon dioxide was desired for the experiments so that the curvature of the sphere would be small enough to be treated as flat.

The modified Stöber method was applied for synthesis 45 nm amorphous silicon dioxide with different hydroxyl density. 10 g Brij58 and 90 mL cyclohexane was charged into a 250 mL three-neck flask and then heated to 50 °C under stirring speed 320 rpm until dissolved. Following 1.5 mL DI H_2O was added dropwise and waited for 30 minutes until fully dissolved. 3 mL ammonium hydroxide solution was added to the solution dropwise and waited 30 mins. Finally, 10 g tetraethyl orthosilicate (TEOS) was added dropwise to the microemulsion. Hydrolysis and condensation of the silica precursors was allowed to proceed for 2 hours at 50 ºC under cold water reflux. Precipitated by adding 2-propanol and washed three times by centrifuge and dried under vacuum oven at room temperature. Crushed powder was placed in calcination boats and calcined at 500 ˚C for 2 h under 0.500 SLM (standard liter per minute) air stream to remove the surfactants.

With the aim of getting different surface hydroxylation densities, calcination was followed after drying in oven. The dehydroxylized silicon dioxide was prepared during calcination with 5 ºC/min ramp rate at 1000 ºC for 2 h under 0.500 SLM air stream. The rehydroxylized samples were then obtained by reacting with boiling water at 95 ˚C for 1 h.

All the reagents were added dropwise until well dissolved. Ammonium hydroxylate served as the catalyst for forming silica precursor and due to its easy decomposition at reaction temperature to produce ammonia, relative more amount of ammonium should be added into the solution and cannot stir for too long time before the next step.

The TEM image shown in Figure 4 reveals that the amorphous silicon dioxide is in round shape and its size is around 45 nm with narrow distribution.

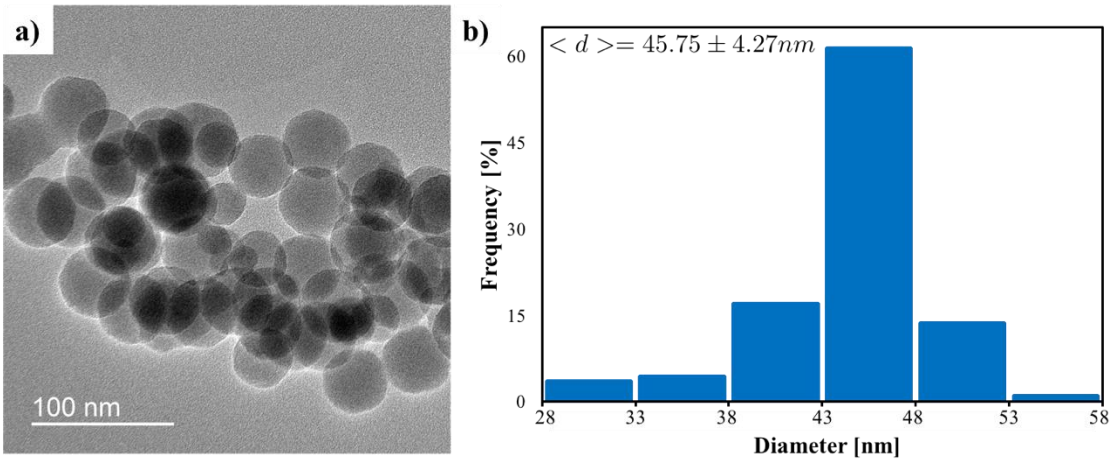

Figure 4 Amorphous supported silicon dioxide of a) TEM images and b) size distribution.

To study the different interactions between platinum and silicon dioxide, two types of SiO_2 of distinctly varied surface hydroxylation degree were synthesized by calcining the SiO_2 samples at 1000 °C for 2 h to remove all surface OH groups. This sample is referred as dehydroxylized silica. Dehydroxylized SiO_2 is then reacted with boiling water followed by drying in vacuum oven at room temperature overnight to obtain the fully hydroxylated (or rehydroxylized) SiO_2.

After synthesis of amorphous supported silicon dioxide nanoparticles in both dehydroxylized and rehydroxylized types, the surface hydroxyl density was calculated by the combination of BET and TGA tests. The detailed measurements and results are discussed in Section 3.2.

During the characterization of surface hydroxyl groups, we find that the silica size (or surface to volume ration) has an impact on the silanol density. Hence, for comprehensive understand the impact of silica size on hydroxyl density, other modified Stöber methods [64] were used to synthesis 6 nm and 100 nm amorphous silicon dioxide samples:

Amorphous silica supports, approximately 100 nm in diameter, were synthesized as following: a solution containing 18 mL of tetraethyl orthosilicate (TEOS, 80.61 mmol), 99 mL of DI water, 36 mL of ammonium hydroxide (30% by volume), and 65 mL of ethanol (190 proof) was mixed at room temperature for 1 hour. The resulting solid was separated from the solution via centrifugation and washed with three times with DI water. Then the samples were dried in vacuum oven under room temperature to remove solvent.

The method used to synthesize 6 nm silica NPs by a two-phase approach of the Stöber method,[64] adapted by Wang *et al,*[65] and further developed by Ewing *et al.*[66] A catalyst stock solution was prepared by mixing ammonia hydroxide solution dropwise to deionized water (500 mL) at room temperature to make the with pH value of 11.4. 34.75 g of catalyst stock solution was charged into a 100 mL round bottom flask, under magnetic stirred, and heated up to 60 °C. 2.8 g of tetraethyl orthosilicate (TEOS, 13.44 mmol) was added to 5 ml of ethanol and stirred completely for about 1 min. After five minutes the TEOS in ethanol mixture was added into the stock solution and reacted for 3 h. Then the mixture was separated by centrifuge, and dried at 50 °C. The dry particles were then calcined at 350 °C and soaked in water for 24 hours at room temperature to get rehydroxylized.

2.2.2 Synthesis of "Unprotected" Platinum Nanoparticles

Metal nanoparticles were usually prepared by forming the metal atoms in the alkaline solution and then protected by some capping agents with large amount of molecular weight such as polymers and surfactants, to aggregate into nanoparticles. With the capping agents, nanoparticles are not only prevented by these protective chemicals from forming large particles, but restrained from interacting with functional groups on the amorphous silicon dioxide surface, for example

the hydroxyl groups. In addition, the final samples are required subsequent removal of capping agents to make the NPs surface functional and accessible for supports. Therefore, calcination under high temperature is necessary, which has strong influences on the surface properties of supports and causes NPs sintering then loss small particle size, as well as catalytic activity.

In order to mimic the simulation condition,[67] which used platinum nanoclusters with 13, 55, and 147 atoms (0.7, 1.2, and 1.7 nm in diameter, respectively), a small size closed to 2 nm of Pt NPs without any added capping agents is desired. Hence, a method of synthesis "unprotected" metal nanoparticles is used in this work. In the absence of capping agents, a suitable solvent, appropriate experimental environment and a controllable method to effectively manipulate small size and narrow distribution of nanoparticles are necessary for the preparation of metal nanoclusters. Previous work of Wang *et al* [68] has established a method using ethylene glycol as the organic solvent to synthesis 1~2 nm metal particles. The preparation procedures of platinum nanoparticles can be expressed by schematic diagram shown in Figure 5:

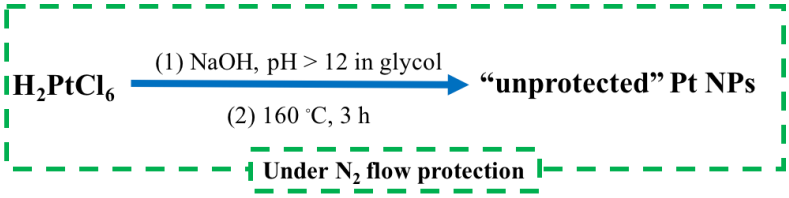

Figure 5 Schematic of platinum nanoparticles synthesis.

An ethylene glycol solution of NaOH (50mL, 0.5 M, dissolved before the reaction) was added into an ethylene glycol solution of $H_2PtCl_6 \cdot 6H_2O$ (1.0 g, 1.93 mmol in 50 mL) with stirring in N_2 atmosphere to obtain a transparent yellow platinum colloidal solution. Then the

mixture was heated to 160 °C for 3 h, with a nitrogen flow passing through the reaction system to take away water and other organic byproducts. A dark-brown homogeneous colloidal solution of the Pt nanocluster (Pt: 3.76 g/L in glycol, 19.3 mmol/L) was obtained without any further treatments. The obtained Pt nanocluster solution is very stable; no precipitate was observed after standing for at least three to four months.

During the synthesis, a critical point is that to keep the pH value of initial solution larger than 12 as reported by Wang. The high pH value can stabilize platinum colloid solution and the further small size. If it is less than 12, a participate will be observed instead of the homogeneous solution. When the NaOH solution and Pt hydroxide solution were mixed, an orange clear mixture was formed within several minutes. By heating up the Pt in glycol solution to 160 °C for 3 h, a transparent dark brown colloid solution was obtained without any participation.

Figure 6 shows the TEM images of small platinum nanoparticles and particle size distribution. The average diameter of Pt NPs (3.76 mg/mL in glycol) is 2.41 nm with narrow size distribution.

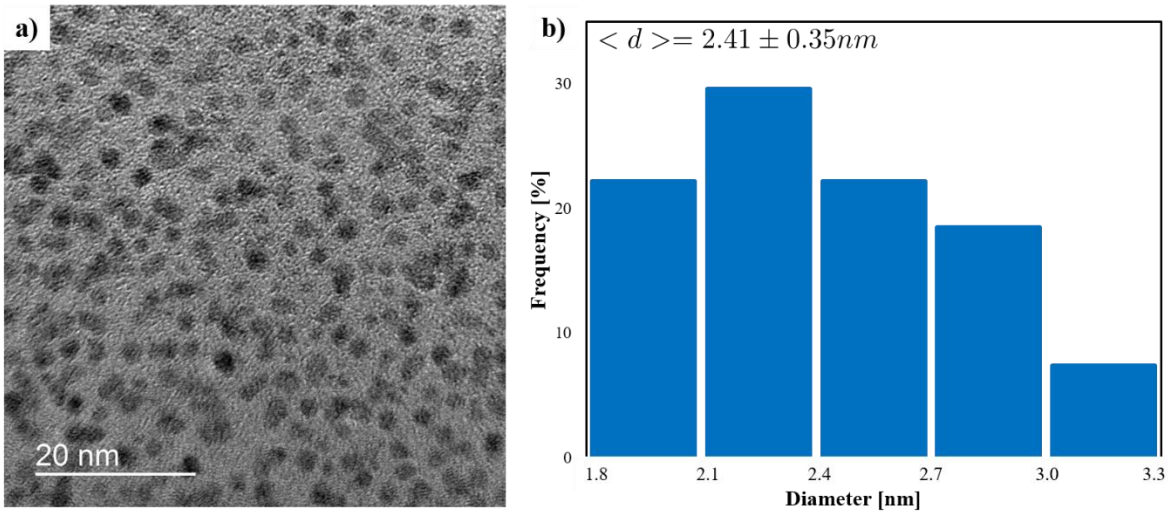

Figure 6 "Unprotected" platinum nanoparticles of a) TEM images and b) particle size distribution.

2.2.3 Synthesis of Pt on Silicon Dioxide Catalysts

240 mg SiO_2 (we used 45 nm diameter amorphous silica as the typical support), 0.637 mL Pt solution obtained above and 15 mL DI water was charged into a 125 mL conical flask and 2.0 g NH_4HCO_3 was added into the solution to get fully saturation under magnetic stirred in room temperature for 30 mins. Quickly added 30 mL 2-propanol into the solution, the light gray precipitate was observed immediately, allowed it to stir for 1h. Then transferred the mixture into centrifuge tubes, centrifuged at 6000 rpm for 5 mins. Washed with 2-propanol for several times. Dried the wet powder in vacuum oven at room temperature overnight to remove water and solvent. Final products can be achieved by calcining the sample at 100 ˚C for 1h under 0.500 SLM air stream to remove the ammonium salts.

2.3 CHARACTERIZATION

2.3.1 Transmission Electron Microscopy Measurements

Transmission electron microscopy (TEM) images were taken on an Environmental-TEM Hitachi H-9500 and JEOL JEM2100F with an accelerating voltage of 300 keV and 200 keV, respectively. Samples for the TEM were prepared by placing a small drop (or small amount of powder) of nanoparticles, diluted in 1~2 mL ethanol, on a copper support grid (from Ted Pella Inc.). Excess solution was removed by the filter paper. Average diameters of NPs were determined using ImageJ from at least 200 nanoparticles found in an arbitrary area in enlarged TEM images. From TEM images, the mean size and size distribution were then calculated.

2.3.2 X-ray Diffraction Measurements

X-ray diffraction (XRD) patterns were obtained by Bruker D8 Discover X-Ray Diffractometer with Cu Kα radiation at 40 kV and 40 mA. Samples were prepared by placing a flat layer of powders on a glass holder. Mean diameters of NPs were determined from XRD peaks patterns using Scherrer equation.[69,70] Calculation of particle size from XRD is the volumetric average diameter of samples.

2.3.3 Brunauer–Emmett–Teller (BET) Measurements

Specific surface area of amorphous silicon dioxide was measured by nitrogen adsorption using the Micromeritics ASAP 2020. The surface area of N_2 was taken to be 1.47 nm^2/mol as determined previously.[71] Samples were degassed at 250 °C for around 6 h. The pore size distributions were derived from the adsorption branches of the isotherms based on the Barett-Joyner-Halenda (BJH) model. The total pore volumes were estimated from the amount adsorbed at a relative pressure of about 0.99.

2.3.4 Thermal Gravimetric Analysis (TGA) Measurements

Sample weight as a function of temperature was measured using a thermogravimetric analyzer (TA Instruments Q600 SDT). Approximately 15~20 mg of sample was heated inside the TGA aluminum pan in a stream of air (20 mL/min) in argon atmosphere (100 mL/min). Three steps

heating procedure was applied to determine the hydroxyls density: (I) heated up to 200 °C at a ramp rate of 10 °C/min; (II) held isothermal for approximately one hour, in order to remove all physisorbed water; (III) heated up to 1000 °C at a rate of 5 °C/min.

2.4 STABILITY TEST SET UP

To test the thermal stability of Pt on silicon dioxide nanocatalysts, a series of experiments were designed using XRD to study the sintering phenomenon. Samples were prepared separately by calcination at different temperature, from 300 to 800 ºC and held 30 mins for each. Calcination process was maintained the same, with a temperature ramp rate of 15 ºC/min. Then the samples were transfered quickly to sample vials and analyzed in XRD in the 2θ range in 30 ~ 90°. Due to the small size of the platinum nanoparticles and low metal loading, a slower scan rate was applied at 1s/step.

2.5 REACTION SET UP

The reaction test was performed in a fix bed reactor. The carbon monoxide oxidation reaction was chosen to be the model reaction. Reaction conditions will be illustrated in latter chapters. A brief schematic flow chart shows below. Powdered catalytic materials were inserted into a 5 mm inner diameter quartz glass tube and was placed within a tube furnace. Both ends of the sample were supported by quartz wool. The temperature in the reaction zone is controlled by the temperature program set in the furnace. Mass flow controllers (MKS Instruments Inc.) were used

to feed reaction gases (CO and O_2) diluted with inert gas (Argon). The products are analyzed by mass spectrometry.

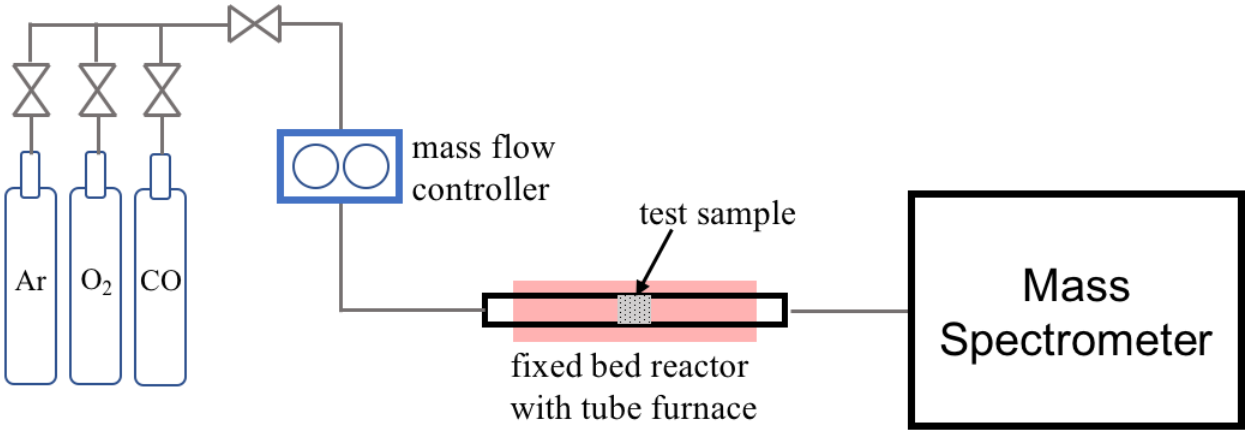

Figure 7 Flow chart of fixed bad reactor setup.

3.0 RESULTS AND DISCUSSION

3.1 MATERIALS SYNTHESIS

3.1.1 Preparation of "Unprotected" Platinum Nanoparticles

Through the "unprotected" platinum synthesis process, the Pt NPs can be stable for several weeks without any precipitation. In fact, the "unprotected" Pt NPs are not bare particles in solution but with the protection from the solvent or simple anions adsorbed on them, or by both. Schrader *at el* [72] shown that the OH−, ethylene glycol, glycolate, and acetate (Figure 8 shows structures and oxidation pathways of ethylene glycol) may act as suitable stabilizers and the latter two have been observed as the oxidation products formed during synthesis.[31,73,74] Through ESI-MS (Electrospray ionization mass spectrometry) and ^{1}H-NMR analysis during the process of the synthesis, glycolic acid (product of first pathway) was confirmed as an oxidation product. The acid will be further deprotonated to glycolate because the alkaline solution. And the corresponding glycolaldehyde structure (medium structure in first pathway) was found as an intermediate formed during the oxidation reaction. In addition, the concentration of the final product of the second oxidation pathway (final product: oxalic acid) could be negligible because it decomposes to CO_2 easily and be too little to act as a stabilizer for the particles.

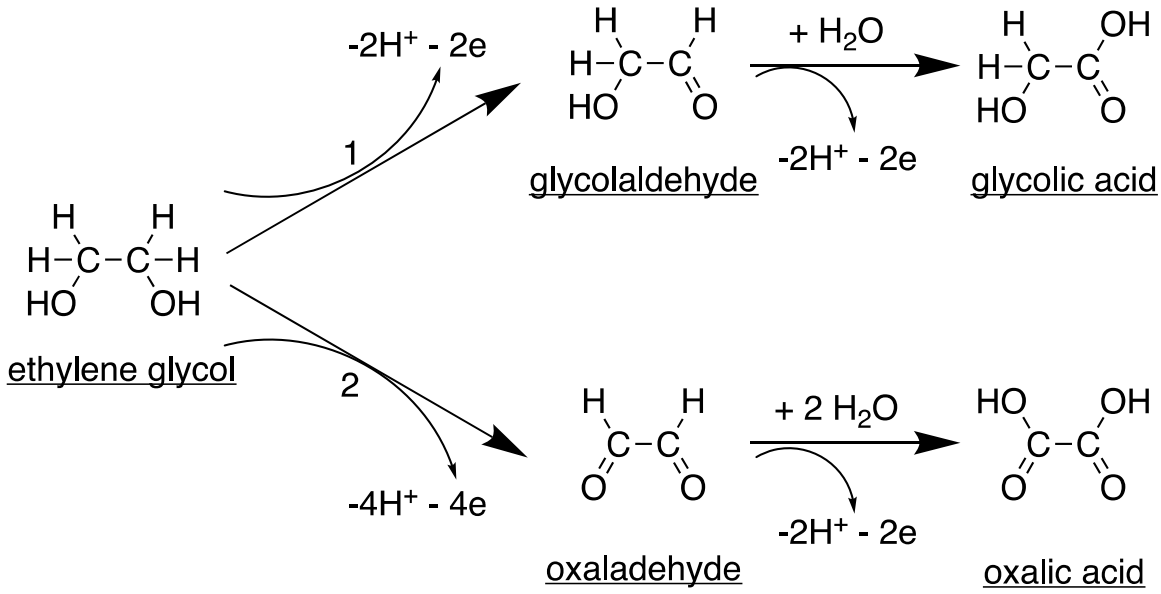

Figure 8 Oxidation of ethylene glycol which delivers the required electrons for the reduction of the metal precursors, proceeding in three different reaction pathways. One of the hydroxyl groups (pathway 1) or both will be oxidized (pathway 2) to C=O.

Since the reaction system consists of OH- also, the possibility of alkaline medium preventing particles growth rises, especially the pH value of the initial solution was noted to reach over 12. It was shown that the presence of OH^- is critical for stabilizing colloids [72] by studied the particle size distribution through SAXS. The influence of the OH^- concentration on the particle size distribution was probed that the size increased and the distribution broadened with the OH^- concentration decreased, but it only influenced into limited change in particle size.

3.1.2 Preparation of Pt Dispersed on Supported Silicon Dioxide

Apart from conventional method to deposit platinum nanoparticles on silicon dioxide by simply physical adsorption, a novel salt recrystallization method was applied in this work.

The salt recrystallization method can be described briefly as follows: a specific salt (principles to choose salt will be expressed later) is added to the mixture with metal and support NPs until the saturated. Then the solvent which the salt has large solubility is added and vigorously stir to accelerate precipitation. The remaining mixture is further purified by centrifugation and the salt is removed by calcination. Finally, we get the NPs separately. The main idea for salt recrystallization is to use salt with low dissociation temperature to bring NPs out of solution by precipitation, and removal of salt at mild temperature leads to same hydroxyl density before and after thermal treatment, which makes big advantages in our work.

In conventional method, NPs in solution are very stable due to whether they are surrounded by capping agents or repulsive between particles which comes from surface ions. Therefore, recovering NPs requires membrane centrifugation. The membrane centrifugation is a tedious, inefficient and time-consuming process. Due to small size of NPs, the pore size of membrane needs to reach nano scale, which introduces much more pressure and time for recovering. Usually for separating 15 mL silica NPs (around 10 nm in diameter) solution requires three hours plus extra time for washing. Additionally, the high concentration of small particles easily blocks the membrane, which makes the process more difficult to achieve.

Using a salt with relative low dissociation temperature, the synthesis can proceed much faster than conventional syntheses. To avoid changing hydroxyl groups density of SiO_2 surface during removal of the salt, ammonium bicarbonate was chosen in synthesis since it dissociates at the temperature of 36 °C at normal atmosphere, which allows complete decomposition of the salt

when calcining the samples at 100 °C. Furthermore, this salt has high solubility in water (21.6 g/100 mL at 20 °C) but is insoluble in 2-propanol which can bring the nanoparticles out of solution as the precipitants through recrystallization simply by adding 2-propanol into the solution.

The Pt/SiO_2 nanoparticles were dispersed roughly using mortar and pestle. Since the Pt particles were "unprotected" by capping agents, there was no need for further calcination at higher temperature. This benefited not only in using fewer steps and less time, but maintaining the similar hydroxyl groups density as measured in the SiO_2 synthesis part.

Figure 9 shows TEM images of 1 wt% Pt/SiO_2 at different magnification from a) to c) and frequency distribution in d) with Pt average diameter 1.55 nm.

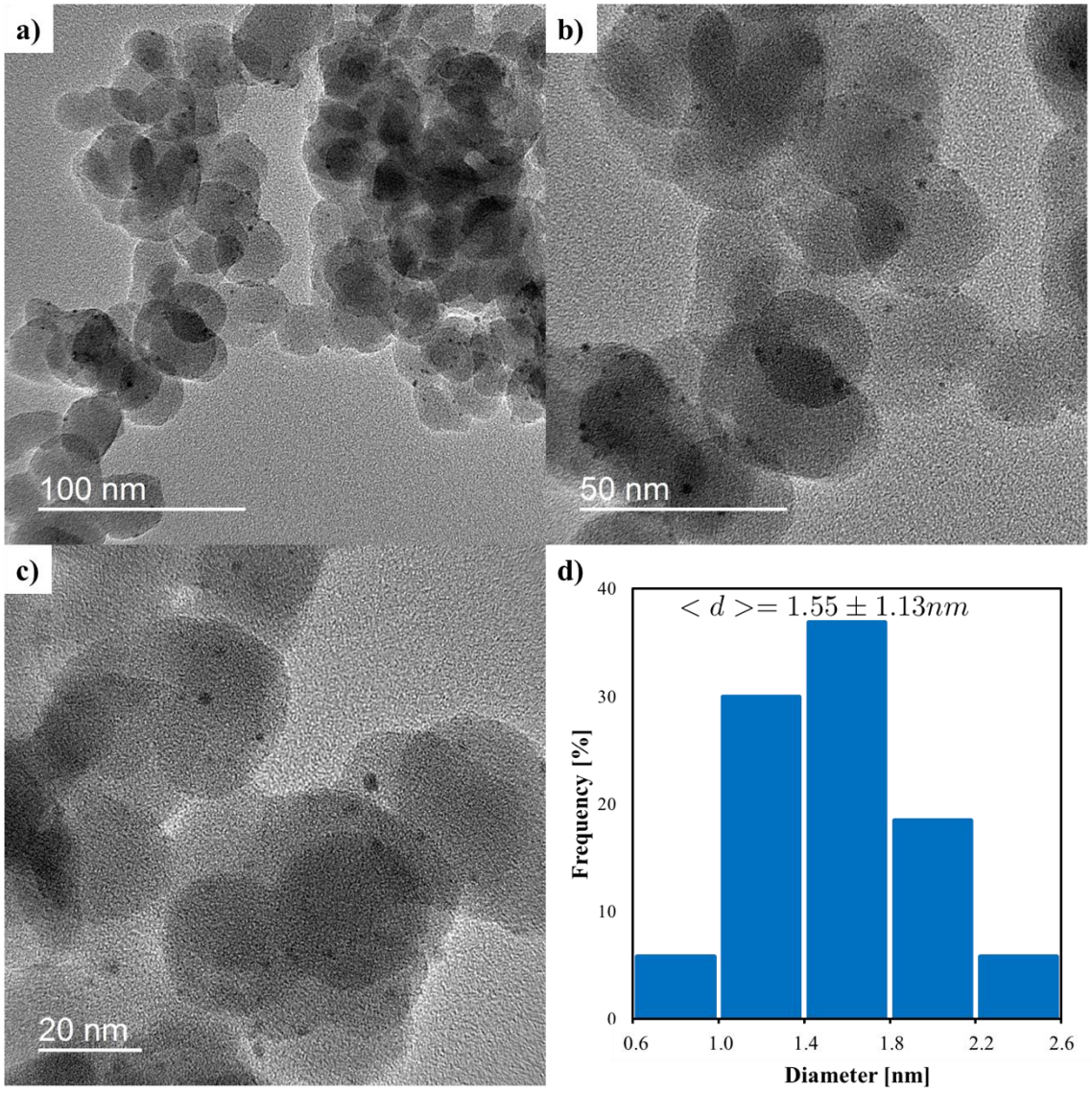

Figure 9 Pt on supported silica nanoparticles of a), b), and c) TEM images and d) Pt NPs size distribution.

3.2 HYDROXYL GROUPS DENSITY CALCULATION

3.2.1 Methods to Determine Hydroxyl Groups Density

3.2.1.1 Deuterium-Exchange Method

The first systematic study of hydroxyl groups density calculation by experiments was published by Zhuravlev [75] on 1973. He introduced the deuterium-exchange method (DE method) [36,76–79] measured by mass spectrometric analysis method (MTA) in conjunction with temperature programmed desorption (TPD) for determining the hydroxyl groups on the surface of dispersed oxide adsorbents. According to this method, an unknown quantity of hydroxyl groups on the surface of the sample was replaced by a known amount of D_2O in isotopic exchange (see Figure 10).

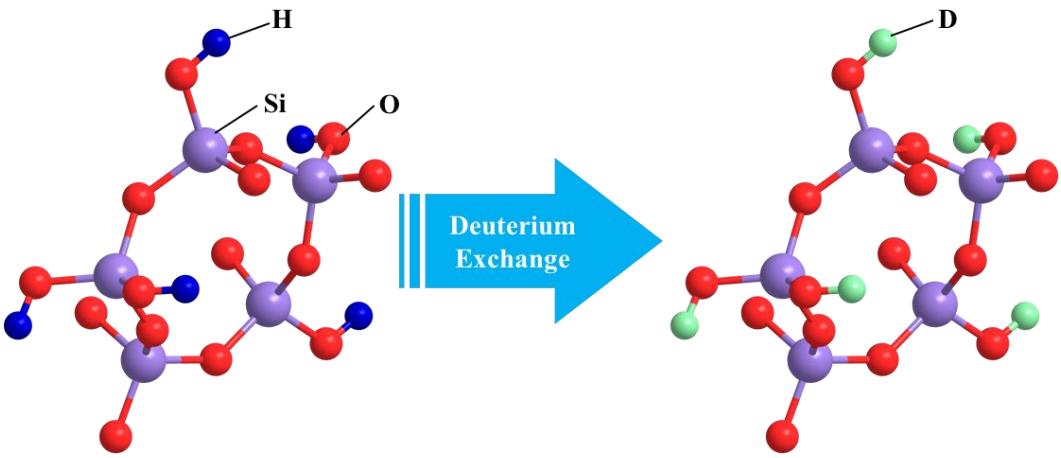

Figure 10 Schematic of deuterium exchange (DE) method. Every H atom (dark blue) would be exchanged by D atom (light green).

The density of the surface OH groups (α_{OH}) is quantified by the mass spectrometer from the ratio of the concentrations of the isotopes: H/D, in the water vapor phase after completion of the deuterium exchange. The main advantage of the DE method is that only hydroxyl groups from surface could participate into isotopic exchange reaction. However, the structural water (or hydroxyl groups) inside the silica particles does not. The major drawback of this method is that it demands much more time and efforts for reaching equilibrium of deuterium exchange and measuring using mass spectrometer. Expensive materials such as deuterium oxide participated in this process also limits its wide usage.

3.2.1.2 Titration Method

The titration method estimating the number of surface OH group was first introduced by Yuasa *et al.* and then developed by Kang.[80,81] The surface hydroxyl density was achieved as following: a known weight of silica sample is soaked with certain amount of NaOH aqueous solution to saturate silica surface with OH anions overnight. The inorganic compounds were separated through centrifugation. Then the above solution was analyzed and titrated until neutralization with aqueous solution of HCl. Then above procedures were duplicated with blank solution. The difference between amount of the HCl solution in blank sample and NaOH soaked sample can be used to calculate surface hydroxyl density. However, this method cannot reach high accuracy due to the limitation of volume accuracy of titration closes to 0.01 mL, which also indicates that a large enough amount of samples required for saturation with NaOH. Besides that, the concentration of acid and base solution needs to be carefully quantified before titration.

3.2.1.3 Thermogravimetric Analysis (TGA) Measurement

According to previous study by Zhuravlev,[39,77–79,82] the process of silica dehydration (i.e. removal of physisorbed water) was complete around 190 ± 10 ºC and the dehydroxylation also began around this temperature. Hence, the weight loss of the silica above 200 ºC is caused by the removal of hydroxyl groups bonded strongly on the surface and in the silica bulk. Thermogravimetry [32,83–85] is recognized as efficient method to determine the hydroxyl groups density on silica surface assuming that water loss during heating up due to the condensation of silanol groups (see Figure 11) and no other elements are escaped from the surface. Therefore, OH density in silica can be calculated from the weight loss percentage during the increasing atmosphere temperature.

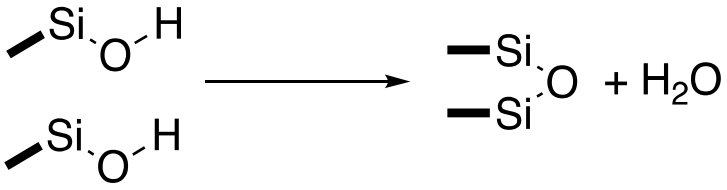

Figure 11 Schematic of amorphous silica dehydration reaction. Each water molecule formed with the presence of two silanol groups on the silica surface needed.

The sample preparation for TGA analysis is simple, small amount of samples is needed (10~20 mg) after calcination or rehydroxylation and also TGA is recognized as an efficient but inexpensive method for determine the hydroxyl density. Compared with DE method and titration

method, TGA provides sufficient accuracy of weight loss and less effort gathering data. Thus, TGA method combined with BET was applied to gather the hydroxyl groups density and the equation for calculation will be illustrated in 3.2.2.

3.2.2 Hydroxyl Groups Density Calculation

The hydroxyl groups density, which also called silanol number (α_{OH}), is defined as the number of silanols per square nanometer. This number can be calculated at different temperature *T* following equation:

$$\alpha_{OH} = \frac{2 \times \Delta wt\%_{H_2O} \times N_A}{SA \times MW_{H_2O} \times 10^{18}} \qquad \textbf{Equation 1}$$

where $\Delta wt\%_{H2O}$ is the sample weight percentage change at temperature T compared to the mass of sample at 900 °C, N_A is the Avogadro number (6.022×10^{23} mol^{-1}), *'2'* in the numerator indicates that one mole of water is formed by combination of two hydroxyl groups, *SA* is the specific surface area which got by BET measurement, MW_{H_2O} denotes the molecular weight of water (18.015 g/mol), and $'10^{18}'$ is the unit transfer coefficient (square meter to square nanometer).

We assumed no silanols were present at temperatures greater than 900 °C. Previous experimental studies have indicated that the density is much less than one at temperatures greater

than 900 °C.[39] Therefore, the assumption has little effect on the quantitative value of the density and does not affect the qualitative features of the hydroxyl groups density curve.

The relation of silanol number (α_{OH}) with temperature was performed using silicon dioxide NPs with diameters of 6, 45m and 109 nm, respectively, and the results are shown in Figure 12. Blue dashed lines indicate the experiment data region from Zhuravlev. They investigated 16 pure amorphous SiO_2 samples having different synthesis origins: silica gels, aerosils (pyrogenic silicas), aerosilogels and porous glasses, and specific surface areas spanning 9.5 – 905 m^2/g, which are indicated as dark blue dots in the figure. The solid lines express the calculated silanol numbers versus temperature from this work and for different silica sizes.

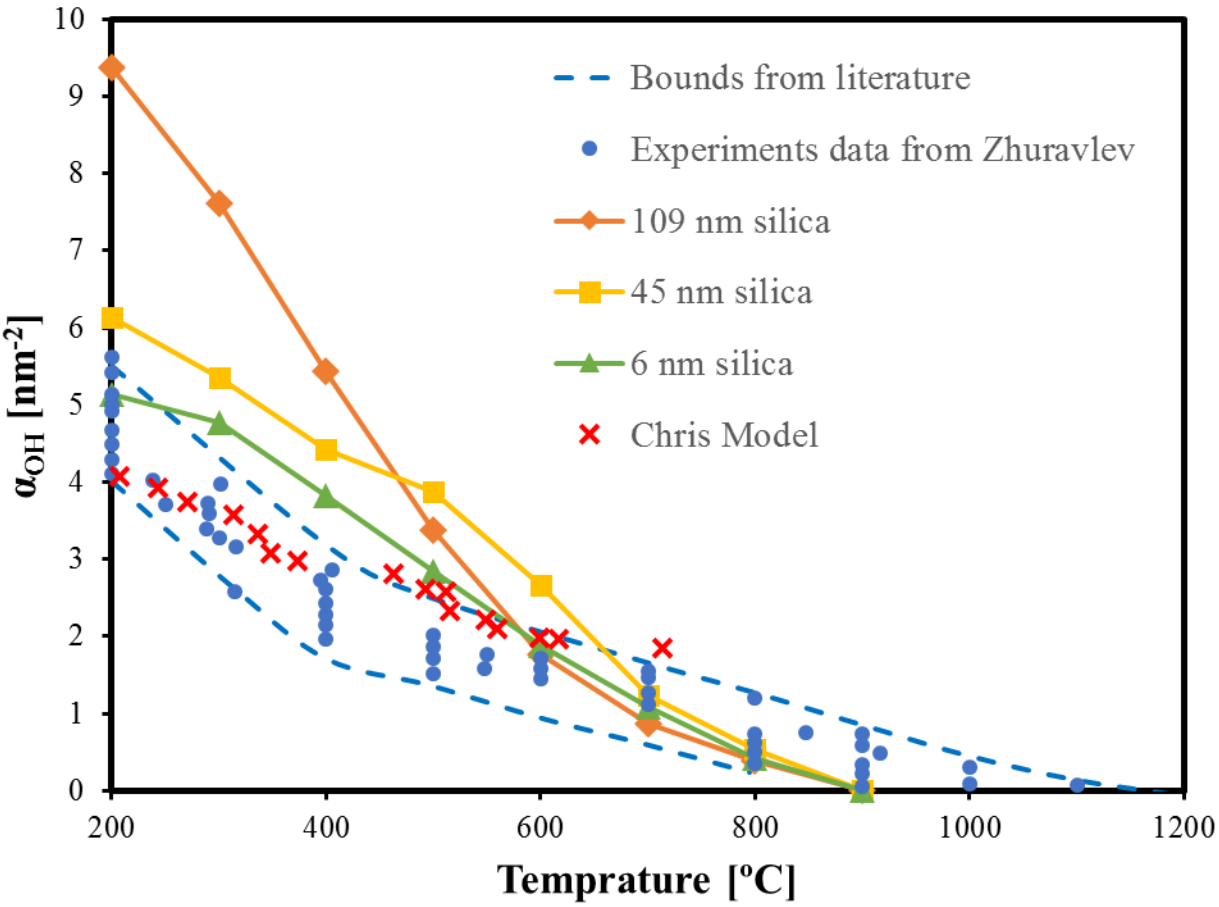

Figure 12 Silanol number as a function of the pretreatment temperature of amorphous SiO_2 (solid lines), modeling data from Ewing work [66] (red cross), experiments data for 16 samples having different synthesis procedures and specific surface areas spanning 9.5 – 905 m^2/g (dark blue dots), and their data bounds (dashed line).[86]

It is obvious that our experimental data more closely approximates the Zhuravlev line as the diameter of silica particles decreases. For example, the silanol number is twice as high as the 6 nm sample at 200 ºC for 109 nm silica. This is caused by the BET method is limited in measuring the surface area of silica bulk structures. The specific surface area of a powder is determined by physical adsorption of liquid N_2 on the surface of the solid and by calculating the amount of adsorbate gas corresponding to a monomolecular layer on the surface. For large silica

samples, this method can only be applied to the micropores or nanopores connected to surface. Instead, encapsulated pores are undetectable because the adsorbate gas molecules cannot get through the silica bulk. However, both hydroxyl groups from surface and inside the bulk structure can be removed under 1000 °C calcination from TGA analysis. Hence, the actual specific surface area would be larger than indicated by N_2 sorption, and hydroxyl density hence will falsely appear higher for large silica particles than for smaller ones. The hydroxyl groups within the skeleton and encapsulated pores can be formed in several ways. For example, in the case of colloid silica forming in an alkali solution, sodium atoms adsorb on silica surface with the silica precipitation, and this process favors silica structure to capture hydroxyl groups.[37] What's more, hydrothermal treatment which is used in widespread applications also causes the bulk inside hydroxyl groups. Gorelik et al. synthesized a series of silica gel using hydrothermal treatment and found the hydroxyl groups inside of the silica structure were contained in these materials.[87] Previous work has shown that TGA together with BET method measured the total concentration of all silanol groups on the surface and in the bulk of silica if the silica contained encapsulated pores.[78] The hydroxyl density for the same silica reached to 8.29 OH/nm^2 for total concentration of silanol groups, otherwise, the surface silanol density was only 4.90 OH/nm^2. While the smallest silica NPs hence minimize this effect, the 45 nm silica particles were chosen for further experiments since they already give reasonably good agreement with the expected curve and have a sufficiently small curvature (in comparison to the ~2nm Pt NP) to approximate a flat silica surface.

3.3 THERMAL STABILITY OF CATALYSTS

3.3.1 Sintering Mechanism of Metal-supported Nanocatalysts

A major challenge for metal-supported nanocatalysts is the harsh conditions during catalytic reactions such as high temperature and longtime exposure under reaction gases. Thermal processes lead to deactivation of catalysts in several ways, for example, it will decrease metal surface area due to agglomeration of catalyst nanoparticles and loss of supported surface area and pore collapse. This phenomenon is referred to as sintering or thermal aging.

Understanding the mechanism of catalysts sintering is a key step in design strategies for catalysts synthesis with better stability. In the field, there is well accepted agreement that sintering of supported metal nanoparticles can occur in two principal mechanisms: (a) atomic migration or Ostwald ripening, and (b) particle migration and coalescence or Smoluchowski ripening. Figure 13 shows a schematic of these two sintering mechanisms. Previous studies have investigated the sintering mechanism via in-situ observation of particles. Stone *et al.*[88] reported a scanning tunneling microscopy (STM) study of Pd NPs on TiO_2, which shows that the sintering is dominated by particle migration and coalescence at temperatures up to 500 ºC. Besides, in situ transmission electron microscopy (TEM) by Baker *et al.*[89] also proved the migration of nanoparticles resulting in coalescence and sintering. The driving force of both mechanisms for nanoparticle sintering is to minimize total surface energy through forming larger particles with less undercoordinated atoms sites.

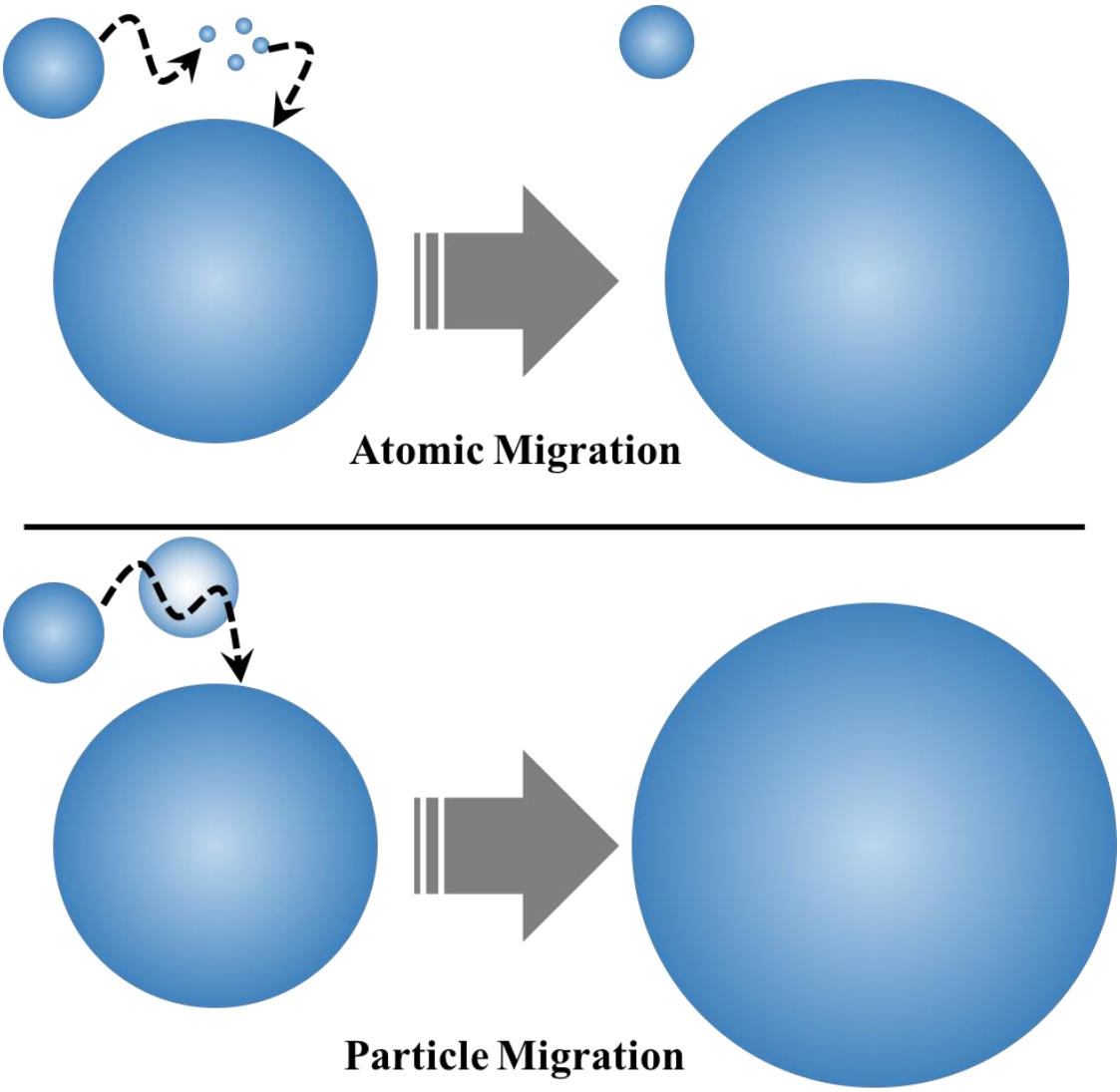

Figure 13 Simple schematic of particles sintering mechanisms: atomic migration or Ostwald ripening (up), and particle migration and coalescence or Smoluchowski ripening (down).

Sintering by particle migration and coalescence relates with Brownian motion of particles on the surface, promoted by relatively weak particle support interactions, and results in coalescence when two particles closely get together. In contrast, Ostwald ripening is described as atoms from smaller particles being transported to larger ones either through surface diffusion on the support or via the vapor phase due to the size-dependent differences in surface energy. In this

case, governing process between dissolving and growing particles is atomic mass transport, during which atoms detach from small particles in high chemical potential, diffuse over the support surface, and consequently attach to larger particles with lower chemical potential [17] . Ostwald ripening can have two different limiting steps: (a) detachment of the atoms from smaller particles (metal interface controlled), and (b) diffusion of the detached atoms on the surface of the support (diffusion-controlled).

Whether atomic migration or particle migration happens depends on the energetics of the catalyst system, such as energy barriers for atom detachment, atomic diffusion over the support, and chemical bonds of metal and supports. There are several conditions under which particle migration is more dominant over atomic migration, such as when the metal-support interaction is low enough that the support cannot grip the metal particles strongly, these particles are prone to move and hence become mobile on surface. Hence, they favor leaving the support and have more opportunities to coalescence with other particles.

3.3.2 Sintering Behavior of Platinum Nanocatalysts

In this work, supported surface hydroxyl groups are assumed to be the critical point to influence the stability of Pt on silica nanocatalysts. Campbell and coworkers shown that the sintering rate is directly related with the NP chemical potential no matter which sintering mechanism dominates the process.[58,59] And this chemical potential is further related with adhesion energy between metal NPs with the supports. Ewing's Pt on silica model concluded that the adhesive energy and net charge are linearly related with the number of Pt-silica bonds (i.e. Pt-O-Si bonds), which can be determined by the NP geometry and surface hydroxyl density, formed during the adsorption of Pt NPs on the silica surface.[63]

To confirm the impact of Pt-silica bonds on thermal stability of $Pt@SiO_2$ catalysts, two different samples with Pt dispersed on dehydroxylized (low hydroxyl density and thus few Pt-silica bonds) and rehydroxylized (high hydroxyl groups and thus more Pt-silica bonds) silica were studied via X-ray powder diffraction (XRD) to obtain volumetric average size of metal particles. Figure 14 shows the XRD patterns of samples pretreated under thermal calcination from 300 to 800 ºC in air. Average particle size was calculated by Scherrer equation using the full width at half maximum (FWHM) of Pt (111) peak at around 39°.

$$\tau = \frac{K\,\lambda}{\beta\,cos\theta} \qquad \textbf{Equation 2}$$

where τ is the mean size of the particles, *K* is a dimensionless shape factor, with a value close to unity. The shape factor has a typical value of 0.94, but may vary with the actual shape of particles. In this work, the value is chosen to be 0.94 since it is already a good approximation based on the sphere morphology of Pt NPs we used.[90] λ is the X-ray wavelength, β is the full width at half the maximum intensity (FWHM), after subtracting the instrumental base line and θ denotes to the Bragg angle. Calculated results are shown in Figure 15.

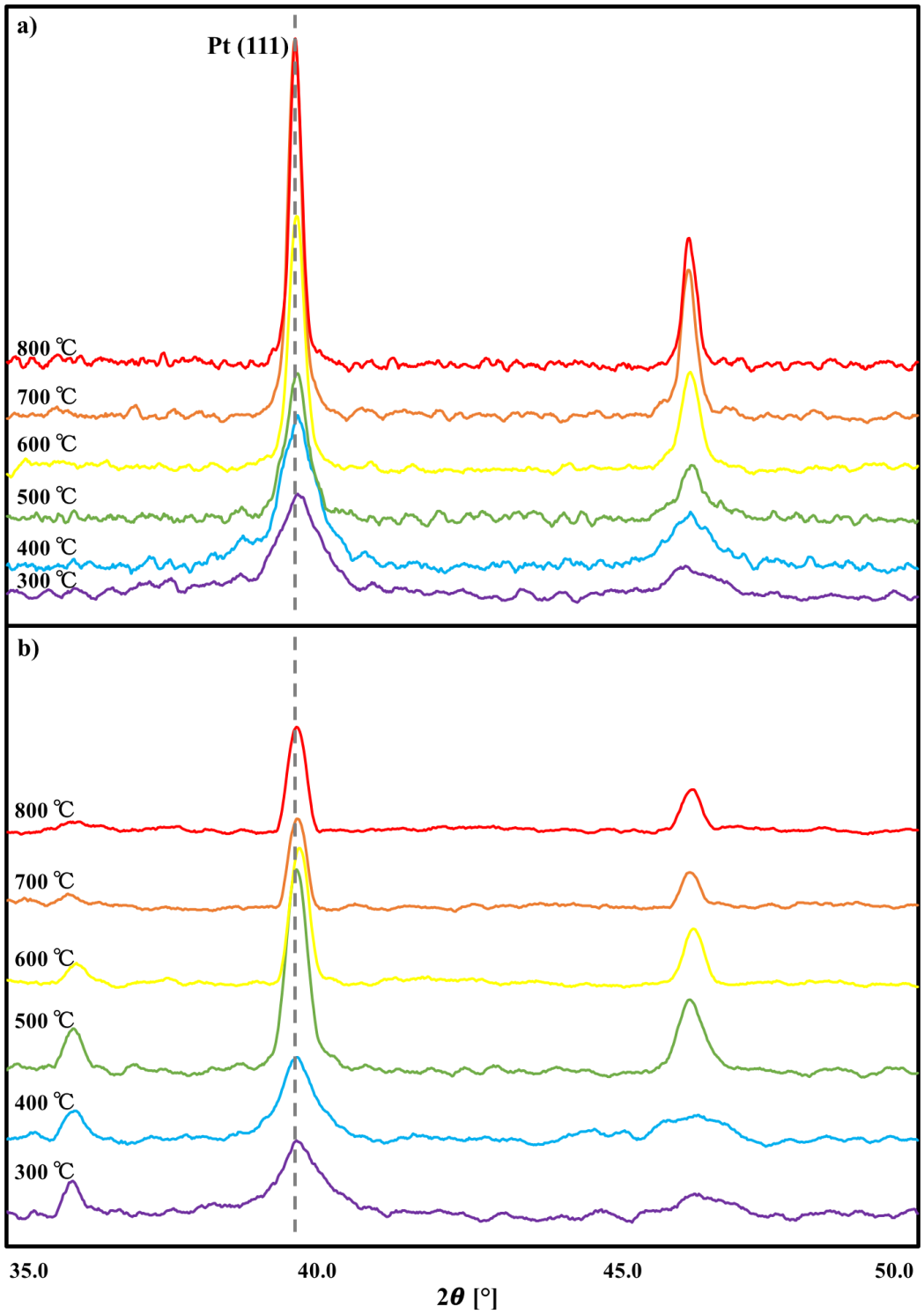

Figure 14 XRD patterns of a) Pt@dehydroxylized silica surface, and b) Pt@rehydroxylized silica surface. Peak highlights in gray dotted line comes from Pt (111). Different colors show different pretreatment temperature from 300 to 800 ˚C, which lists on the left side above each pattern (color varies from purple to red).

In general, the particle size grows as the pretreatment temperature increases. At lower temperature, from 300 to 500 ºC, the growing speed of particles of two samples is nearly identical. The Pt particles grow from 11 to 20 nm in average size, which indicates similar sintering happened for both catalysts. However, the sintering behavior varies a lot for two samples after 500 ºC. The dehydroxylized silica (orange line) keeps the high sintering speed and grows further to around 40 nm. In contrast, the rehydroxylized silica (blue line) slows down and seems to stabilize at ~ 26 nm even under 800 ºC.

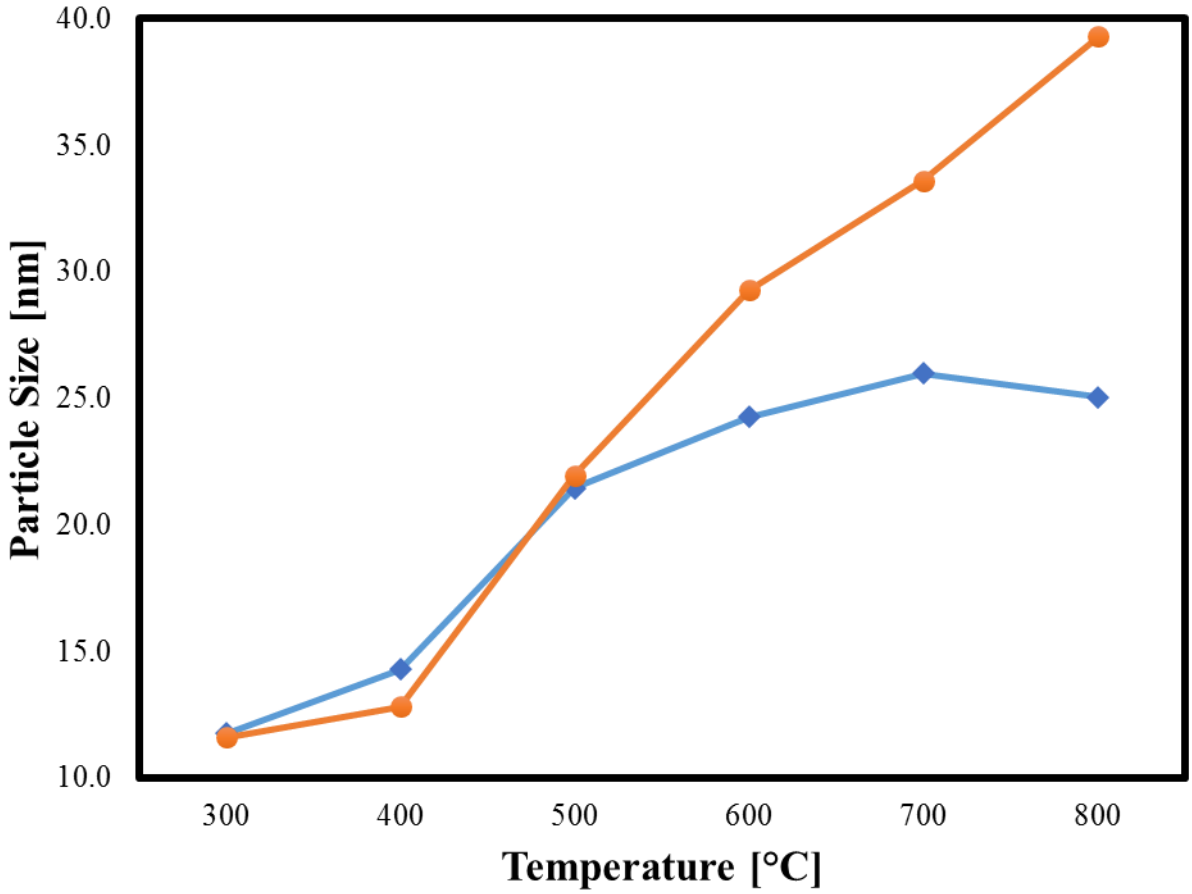

Figure 15 Average particle size grows with pretreatment temperature via XRD and calculated by Scherrer equation with Pt (111) peak information. The samples were pretreated in calciner under corresponding temperature at same ramping speed and calcined for 30 mins. Orange and blue lines indicate the samples of Pt nanoparticles dispersed on dehydroxylized silica and rehydroxylized silica, respectively.

The divergent sintering behavior at relatively higher temperature (over 500 ºC in this case) indicates the sintering process would be different for the dehydroxylized and rehydroxylized samples. From considerations of energy aspect, particle migration and coalescence are dominating sintering at moderate temperatures due to the energy needed for

moving a metal atom from the particle to the surface of the support is high, which is around the same energy as the heat of sublimation of metals,[91] for example, 565 $kJ \cdot mol^{-1}$ for Pt.[92] But the energy of platinum atoms adsorbed on a Pt particle surface is much lower than the energy of atoms absorbed on the supports, which implies that the atomic migration mechanism is unfavorable at moderate temperature. In this work, XRD results show the similar trend of particles' growth for rehydroxylized and dehydroxylized samples at the temperature lower than 500 ºC, which may suggest they undergo the same particle migration mechanism.

However, focusing on the particle size of each sample at different temperature, a series of unreasonable values should be noticed that the NPs grown to 11 nm even for sample calcined under 300 ºC, especially compared to the small size (1~2 nm in diameter) of Pt on fresh catalysts (no calcination after synthesis). Three samples from different pretreatment temperature: 300, 600 and 800 ºC were characterized by TEM to confirm the trend of particle size. Figure 16 shows the TEM images and its corresponding particle size distributions for both rehydroxylized and dehydroxylized catalysts in different calcination temperatures. It is explicitly that there are some differences in average diameter of the particle calculated by images with the diameter estimated by XRD for both rehydroxylized and dehydroxylized samples. For dehydroxylized catalysts, the average particle size grows to 13 nm while the size is 40 nm got from XRD. This is mainly caused by several reasons: one is the error from characterization equipment itself. XRD has less sensitivity of small particle size (usually around 3 nm, depend on materials), combined with low metal loading (1% wt in this case) of the samples, it is hard to calculate the crystallite size accurately.

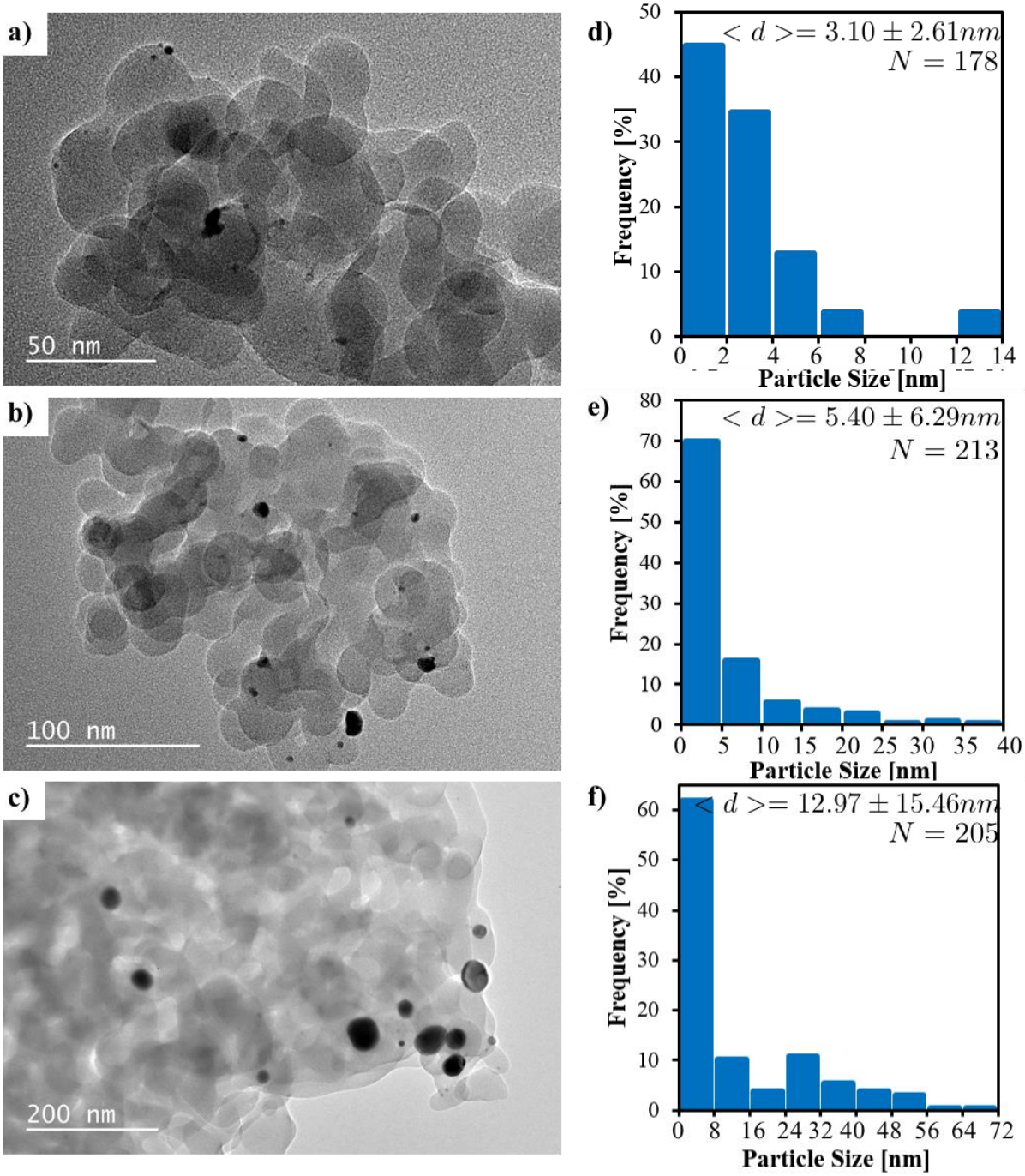
a)
50 nm
b)
100 nm
c)
200 nm
d)
$< d >= 3.10 \pm 2.61nm$
$N = 178$
Frequency [%]
Particle Size [nm]
e)
$< d >= 5.40 \pm 6.29nm$
$N = 213$
Frequency [%]
Particle Size [nm]
f)
$< d >= 12.97 \pm 15.46nm$
$N = 205$
Frequency [%]
Particle Size [nm]

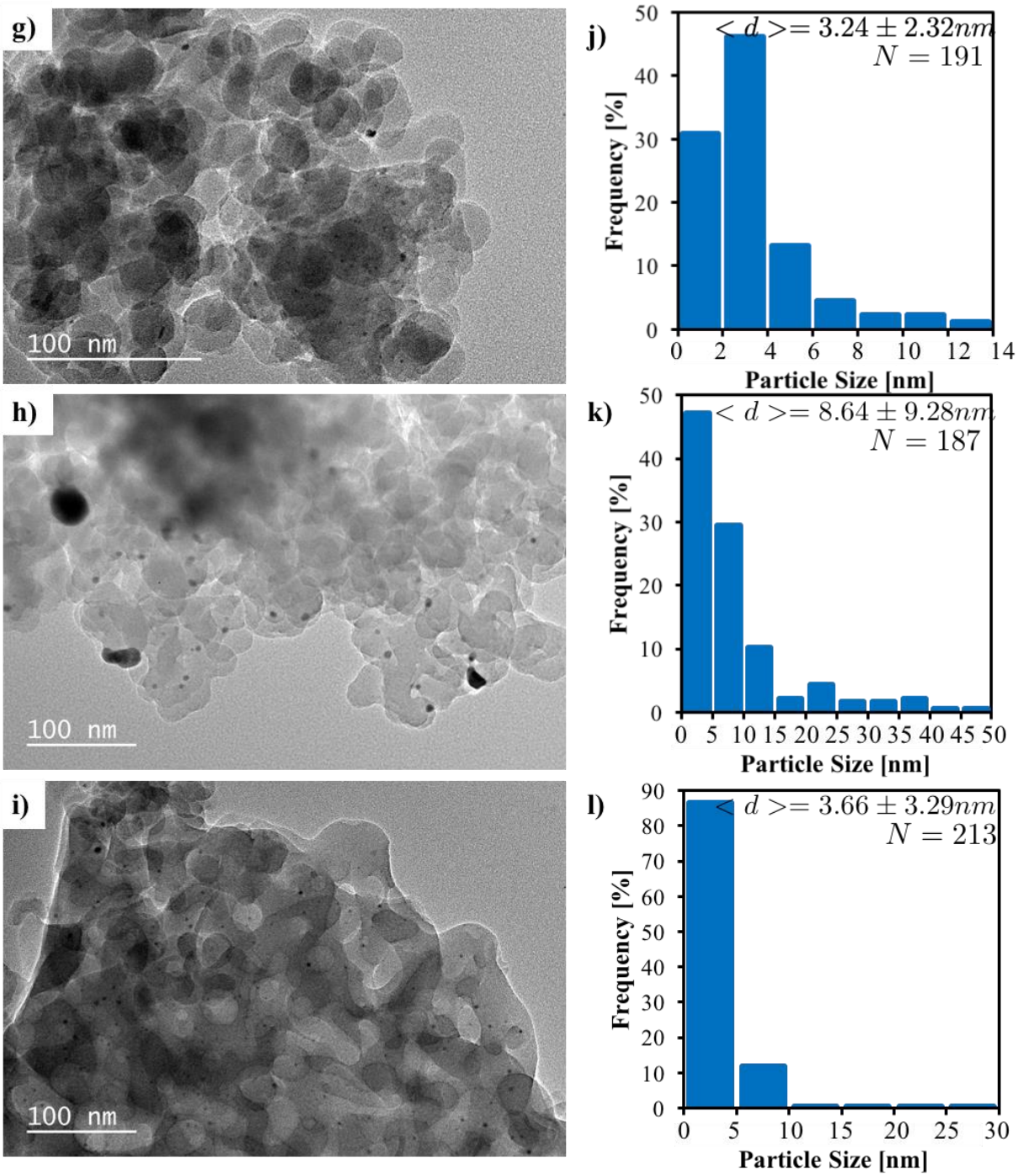

Figure 16 TEM images (a~c, g~i) and corresponding particle size distribution (d~f, j~l) of dehydroxylized sample (from a to f) and rehydroxylized sample. Calcination temperature varies from 300, 600 to 800 ºC (from up to bottom).

Another important reason is that XRD provides an average particle size from a volume average across the whole sample other than number average. Table 1 shows the volumetric average diameter calculated as equivalent length by considering all the particles observed in TEM images into one particle (equation shows below).[93]

$$d_{mean,vol} = \frac{\sum_i^N d_i V_i}{\sum_i^N V_i} = \frac{\sum_i^N d_i \frac{4}{3}\pi(\frac{d_i}{2})^3}{\sum_i^N \frac{4}{3}\pi(\frac{d_i}{2})^3} = \frac{\sum_i^N d_i^4}{\sum_i^N d_i^3} \qquad \textbf{Equation 3}$$

Where $d_{mean,vol}$ is volumetric average size of particles, d_i are diameters measured for N individual particles from TEM images, V_i is the volume of each particle.

Table 1 Average size calculation summary of Pt NPs under different pretreatment temperature for dehydroxylized and rehydroxylized catalysts based on length average and volume average.

Sample	Pretreatment Temperature [°C]	Average Diameter from XRD [nm]	Average Diameter from TEM [nm]	Volumetric Average Diameter Calculated from TEM [nm]
Dehydroxylized Catalysts	300	11.60	3.10	11.24
	600	21.95	5.40	24.68
	800	39.28	12.97	51.04

Table 1 (continued).

Rehydroxylized Catalysts	300	11.60	3.24	8.94
	600	21.44	8.64	38.72
	800	25.05	3.66	24.08

It is noticeable that average particle size of rehydroxylized catalysts increases up to 8.64 nm after pretreatment at 600 °C but then decreases to 3.66 nm after higher temperature calcination (800 °C), which is not only contrast with the trend obtained by XRD, but oddly abnormal since particles cannot grow smaller with increasing temperature. Detailed studies show that two distinct size groups of metal particles occur on the TEM images of rehydroxylized samples under 600 °C calcination (Figure 16, h and Figure 17). One of the bimodel size distributions consists of small Pt NPs with 1~8 nm diameter, which makes over 80% of all particles (see Figure 16, k), while the other group has the NPs much bigger, from 20 to 50 nm which only takes other 20%. The particle size doesn't follow the normal distribution and exists an obvious gap between these two groups. This diverse size of two groups Pt NPs may suggest that there are two types of Pt on silica. One maintains the small size around 3 nm through thermal treatment, while the other one is unstable and grows bigger. Further calculation of volumetric average size of separated groups (see Table 2) shows that the larger 20% of the particles dominate the XRD particle size estimation results, which incompletely presents the particles growth. Sehested has shown some evidence of that through the sintering process, metal particles were dominated by the particle migration and coalescence mechanism at moderate temperature.[91] Thus, in this work, those unstable platinum particles agglomerate into large

particles with 20~50 nm diameters could undergo particle migration. At higher temperature, unstable group sinters severely and coalesces into bigger particle. Meanwhile, the number of these particles decreases. This could be the reason why we observe much less particles over 10 nm in the TEM for 800 ºC samples since the frequency of those large particles becomes very small. Since TEM characterizes NPs in a small and localized area, even though several areas and hundreds of particles are involved in distribution analysis, the calculation still cannot reflect the whole samples. For catalysts study, the main property we concentrate is the catalytic reactivity of catalysts. Particles maintain over 80% reactivity under high thermal treatment could still be remarkable catalysts with good performance. It is also tedious, time-consuming to measure thousands of particles to obtain a relative comprehensive picture of particle size.

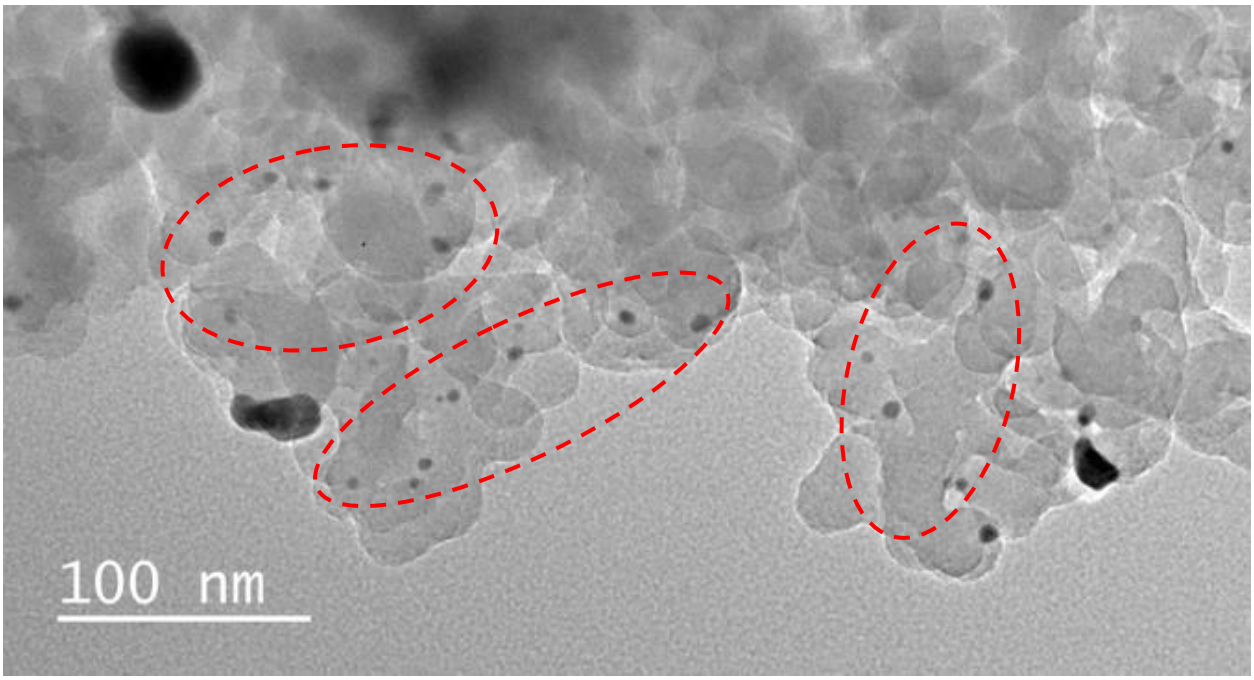

Figure 17 TEM images of rehydroxylized catalysts. There are two obvious groups of particles. Red dash lines indicate the small Pt particles in 1~10 nm while the other group has the diameter over 10 nm. The particle size distribution is not continuous but exists a gap between these two groups. Detailed discussion see text.

Table 2 Modified average size of particles in 300, 600 and 800 °C for rehydroxylized catalysts. Volumetric average size is calculated using the equation above.

Sample	Pretreatment Temperature [°C]	Volumetric Average Diameter Calculated from Particle Size smaller than 10 nm* [nm]	Volumetric Average Diameter Calculated from Particle Size over than 10 nm* [nm]
Rehydroxylized Catalysts	300	6.19	11.96
	600	7.08	39.56
	800	4.80	27.33

* Volumetric average is calculated from bimodel size distributions obtained by TEM. Two groups are separated by particle size less or over than 10 nm.

The differences of two separated particle group at atomic level still need to be carefully studied to investigate the mechanism of varied sintering behaviors. However, due to surface properties of amorphous silica, the bimodal size distribution could be caused by different bonding between silica and platinum particles. For example, the silica surface is actually not fully hydroxylized of every single silica atoms. Therefore, not all platinum particles are bounded with oxygen atoms from hydroxyl groups, those unstable group may consist of most non-Pt-O bound particles. Besides, the adsorption sites on amorphous silica surface is not uniform, which leads to nonuniform dispersed Pt particles.

In conclusion, surface hydroxyl density could be characterized by a combination of TGA and BET method if the silica has non-porous structure inside. Although for amorphous silica with micropores in bulk structure, this method proves that the hydroxyl density could still be

tuned by different pretreatment temperature. Further quantified measurement could also be used in calculating surface silanol density, such as using IR (Infrared spectroscopy) to study the OH vibration peak ($\boldsymbol{\nu}$(OH) = 3741 cm^{-1}) intensity together with the calibration concentration of OH groups, it is possible to determine the OH density only on silica surface.[94,95] The particle size determined from XRD size estimation and TEM images both confirm that the fully hydroxylized catalysts, which contain higher silanol density, have higher stability of most Pt NPs than the dehydroxylized ones as the results of hydroxyl groups stabilize the Pt NPs. Through the process of temperature increases, we observed a bimodal particle growth phenomenon of Pt NPs on dehydroxylized silica. Despite the size growth of Pt particles on this catalyst, it is remarkable that majority of NPs are stable towards high thermal treatment. The reactivity of these highly resistant to sintering catalysts is studied further in following experiments.

3.4 REACTIVITY OF CATALYSTS

CO oxidation reaction over Pt-group metal catalysts is a widespread heterogeneous catalytic reaction investigated by scientists, although one of the simplest reaction process known, plays crucial position in practical and fundamental studies. For example, high demand for clean energy requests minimum concentration of emission from automobile exhaust. Purification of H_2 to remove CO is required for polymer electrolyte fuel cells (PEFCs) since CO is a strong poison to Pt electrodes. In addition, the simplicity of CO oxidation is desired to be a model reaction for surface chemistry studies.[96–101] The reaction operates in two distinct kinetic regimes divided by an ignition temperature. Below this temperature, the catalysts surface is covered mainly by CO. Reaction rate is governed by surface reaction and follows Langmuir-Hinshelwood (LH)

mechanism.[102–105] In a very narrow temperature range, the reaction transition occurs from primarily CO covered to only O_2 covered. The consumption of CO increases dramatically and together with rapid rise in temperature. This process is so called ignition and the temperature required for this defined as ignition temperature. Above ignition temperature, reaction is controlled by mass transport and the reaction rate is limited by either detachment of CO_2 product or approach of CO on surface.[106]

Rinnemo *et al.* [104] found that ignition temperature increases with the increase of CO/O_2 ratio, and the values of temperature on Pt single crystals range from 226.8 to 326.8 °C. McCrea and co-workers shown that both CO oxidation and dissociation processes are structure sensitive.[106] The ignition temperature of CO oxidation at 40 Torr CO and 100 Torr O_2 on Pt(100), Pt(557) and Pt(111) is 226.8, 366.8, and 346.8 °C, respectively. Yang *et al.* studied the effect of sintering of $Pt@Al_2O_3$ catalysts on CO reactivity and found that the catalytic activity for CO oxidation under different CO and O_2 concentrations decreases after aging the catalyst at 600 and 700 °C for several hours.[107]

To investigate the effect of hydroxyl density of support silica under high-temperature catalytic reaction, CO oxidation reaction was used as a model reaction. During the test, we expect to observe the reactivity of catalysts diminishes gradually during the reaction cycles due to Pt NPs sintering at high reaction temperature. For highlighting the reactivity difference after sintering of catalysts, the reaction was cycled three times from room temperature to 650 ºC on both rehydroxylized (with relatively high hydroxyl density on silica surface) and dehydroxylized (low hydroxyl density) catalysts. CO oxidation was carried out with excess O_2 (8 vol% CO, 8 vol% O_2, balanced with Ar) for the propose of using CO conversion as reference standard. Additionally, there exist temperature differences between the furnace, which is used to keep

isothermal for reaction, and the real fix-bed reactor. Figure 18 shows a typical temperature differences by measuring reactor temperature via inserted thermocouple. Blue dash line indicates the ideal temperature in the furnace, which is shown on the control panel. The orange solid line implies the temperature on the catalysts surface in the fix-bed reactor, which is measured by a thermocouple directly inserted in the reactor and touched the solid catalysts surface. Hence, to maintain the reaction under isothermal condition, highly diluted inlet gases (i.e. 84 vol% Ar dilution) were fed to prevent too much heat generated by this exothermic reaction.

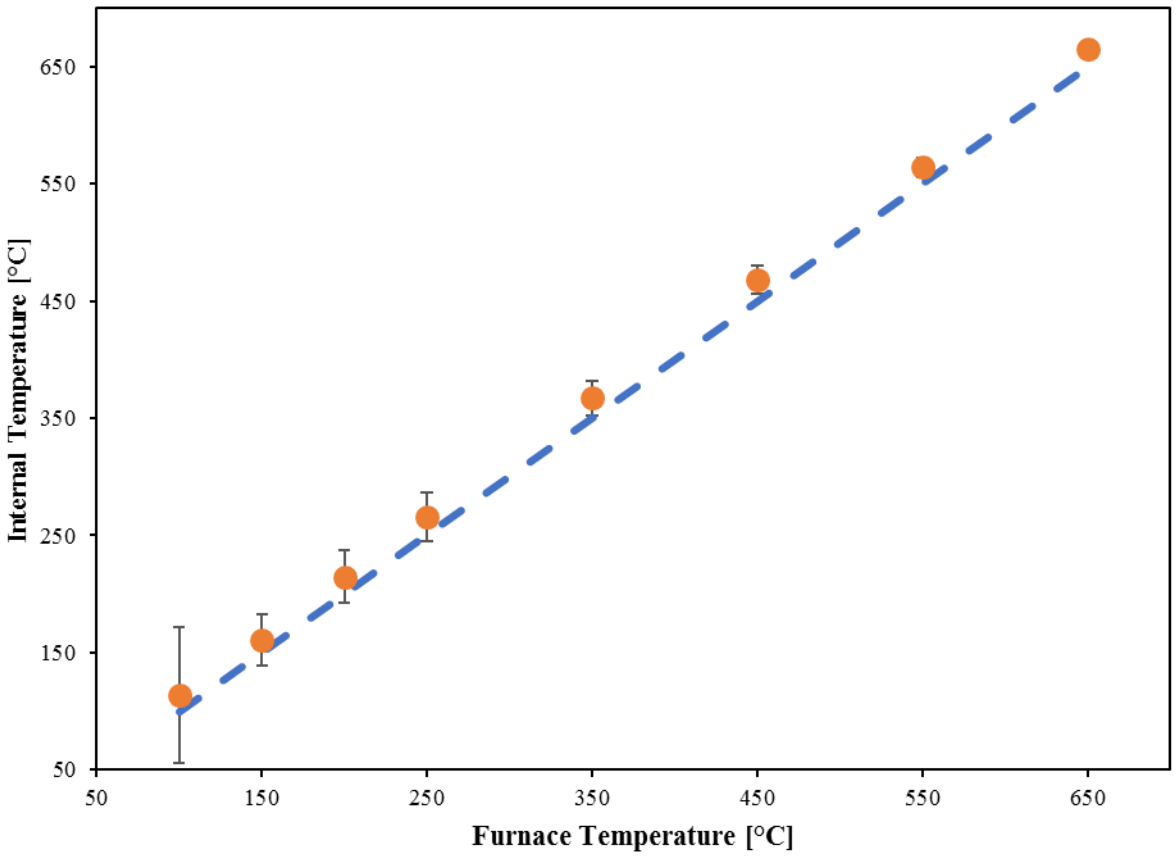

Figure 18 Temperature differences between furnace and internal (fix-bed reactor). Blue dash line indicates the ideal temperature for furnace and reactor, which is controlled by furnace and should be the same as the temperature of catalysts. Orange dots are real temperature measured by thermocouple inserted into fix-bed reactor and touched catalysts surface. The experiment is operated under the same reaction gases (8% CO, 8% O_2, balanced with Ar) as investigated in future by using Pt on dehydroxylized silica catalysts as an example. The inlet gas flowrate and catalysts weight loading maintain the same as further study.

A common phenomenon observed in many exothermic catalytic reaction system called temperature hysteresis was reported in previous study.[108] The hysteresis is described as the temperature of reaction dependences of the conversion (or reaction rate) through temperature

ramping up and cooling down conditions did not coincide. As the temperature increases, the catalysts would be ignited at certain temperature and achieve high conversion due to the external heat reaches the activation energy of the reaction. However, when catalysts cool down, the reaction conversion maintains high since the exothermic reaction would release extra heat and compensate the loos of temperature. In some cases, with a certain ratio of components, the reaction continued to occur with high conversion or reaction rate even after the temperature is dropping. The hysteresis loop consists of two branches: ignition branch (temperature increases) and extinction branch (temperature decreases), and could be characterized by ignition and extinction temperature. Lower extinction temperature compared with ignition temperature is often caused by local overheating of active sites on the catalysts, which due to the excessive reaction heat from highly exothermic CO oxidation (ΔH = 283 kJ/mol).[108] In this work, the reaction results obtained are presented as the dependence of CO conversion vs reaction temperature. The ignition temperature is defined here as the reaction temperature when CO conversion is higher than 80% and calculated through linear regression.

A typical hysteresis figure is shown as Figure 19 for both dehydroxylized and rehydroxylized catalysts. The solid lines are ignition branch and dash lines indicate extinction branch. Different colors of lines show the different reaction cycles. In general, the second and third reaction cycle follow almost identical pathway, which suggests the catalyst has stabilized under reaction conditions. Compared with these catalysts, the trend for ignition and extinction temperature is the same: both temperatures of dehydroxylized catalysts are higher than rehydroxylized ones, indicates that the dehydroxylized catalysts deactivate more severe. Since the major deactivation process in this reaction is the particle sintering, dehydroxylized catalysts with lower hydroxyl density also have lower resistance to sintering.

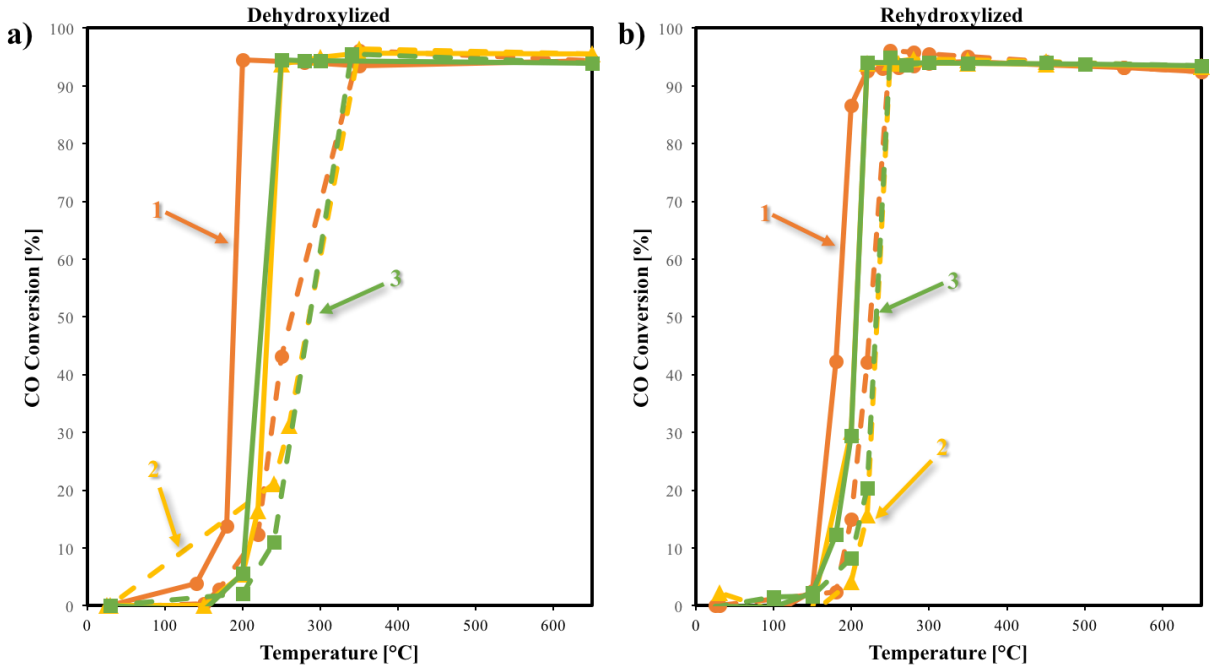

Figure 19 Hysteresis loop of CO oxidation for dehydroxylized (a) and rehydroxylized (b) catalysts. For each catalyst, three reaction cycles are performed under same reaction conditions, and indicated by different colors (orange-yellow-green: 1-2-3). Ignition branches shown as solid lines and extinction branches shown as dash lines.

Comparing the extinction branches, both catalysts extinct at higher temperature than ignition, which is very usual and abnormal. Basically, these high temperatures show that there is no hysteresis of the Pt@SiO_2 catalysts. The reason why extinction behaves unusual is still under further studies. However, we propose that different adsorption states could cause this phenomenon. As reported by Hong, Vlachos and etc, CO oxidation reaction operates in two distinct states separated by an ignition temperature. At low temperature, the catalysts surface is covered mainly by CO. [102–105] When reaction reaches ignition temperature, the transition occurs from primarily CO covered to only O_2 covered. The reaction rate of CO increases and together with rapid rise in temperature. Thus, CO conversion quickly increases, which is so called

ignition. During the reaction temperature cools down, the conversion of CO could still stay at high caused by the exothermic phenomenon of reaction. However, CO covered catalysts would be dominant at lower temperature. In addition, the external temperature keeps cooling. Consequently, the reaction rate drops rapidly and shown as extinction of catalysts at higher temperature than ignition.

To clear comparing reaction results of dehydroxylized and rehydroxylized catalysts, further discussion is only based on ignition branches of two catalysts. However, although the extinction temperature behavior is in doubts, the trend of dehydroxylized catalysts lie in higher temperature correlates with the ignition process.

Figure 20 shows that for both dehydroxylized and rehydroxylized catalysts, the ignition temperature of third reaction cycle increases by about 50 °C and 20 °C compared to the first cycle, respectively. During the first reaction cycle, shown in Figure 21, a, the reactivity behavior is very similar for both catalysts, as evident from the same ignition temperature (197 °C) and maximum CO conversion (~96%). In contrast, comparing the final reaction cycle for both catalysts (Figure 21, b), the ignition temperature of rehydroxylized catalysts remains 30 °C lower than the dehydroxylized ones, which suggests the thermal stability of previous catalysts is higher. This confirms that the high surface hydroxyl density leads to higher thermal stability. The ignition temperature for the last reaction cycle is around 215.6 °C for rehydroxylized catalysts and 241.9 °C for the dehydroxylized samples. Compared with the results from McCrea *et al.* as we discussed initially, ignition temperature of the dehydroxylized catalyst lies in between of Pt(100) (227 °C) and Pt(111) (347 °C) [106] single crystals, it may suggest that there would be more Pt (111) facets than rehydroxylized catalysts after sintering, and the former XRD pattern seems to suggest this by showing much higher intensity increase of Pt (111) peak (compared

with Pt (200) peak at 46°) than the rehydroxylized catalysts. However, the reaction conditions in McCrea's work are different with this work, detailed morphology studies of Pt NPs after sintering are needed. Reaction summary including the conversion and ignition temperature for three reaction cycles is shown in Table 3.

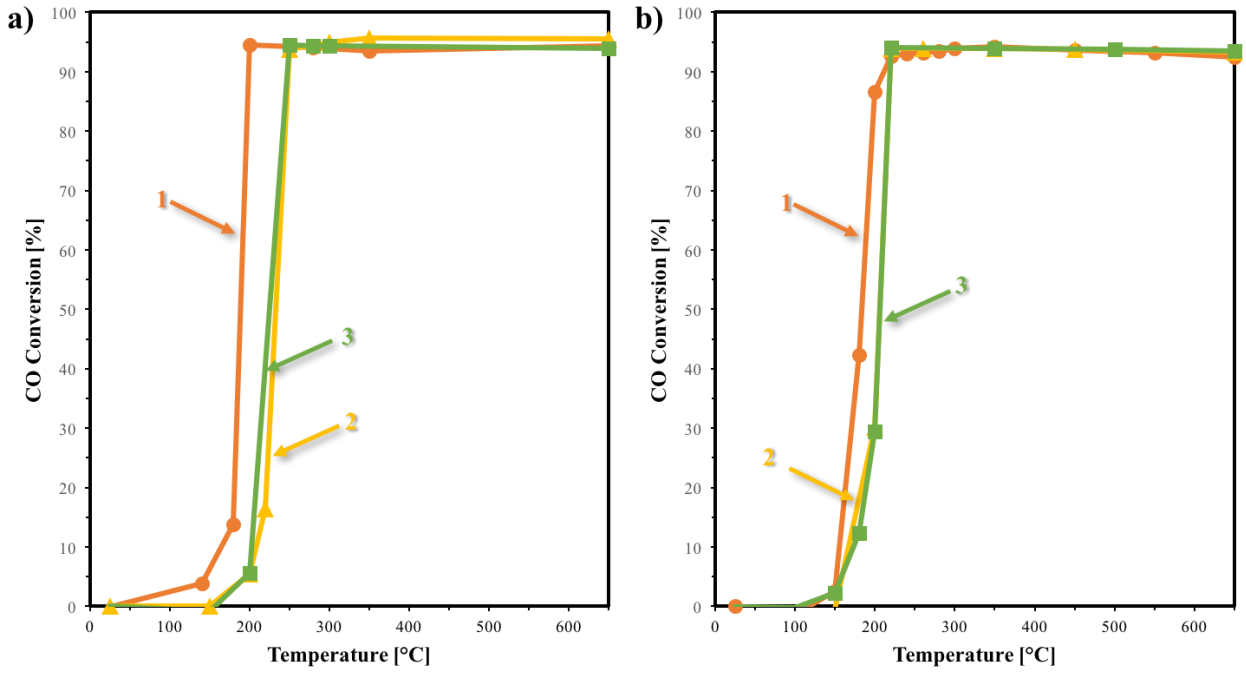

Figure 20 Temperature dependence of CO conversion of dehydroxylized catalysts (a) and rehydroxylized catalysts (b) for three reaction cycles, indicated by the number and arrow close to lines.

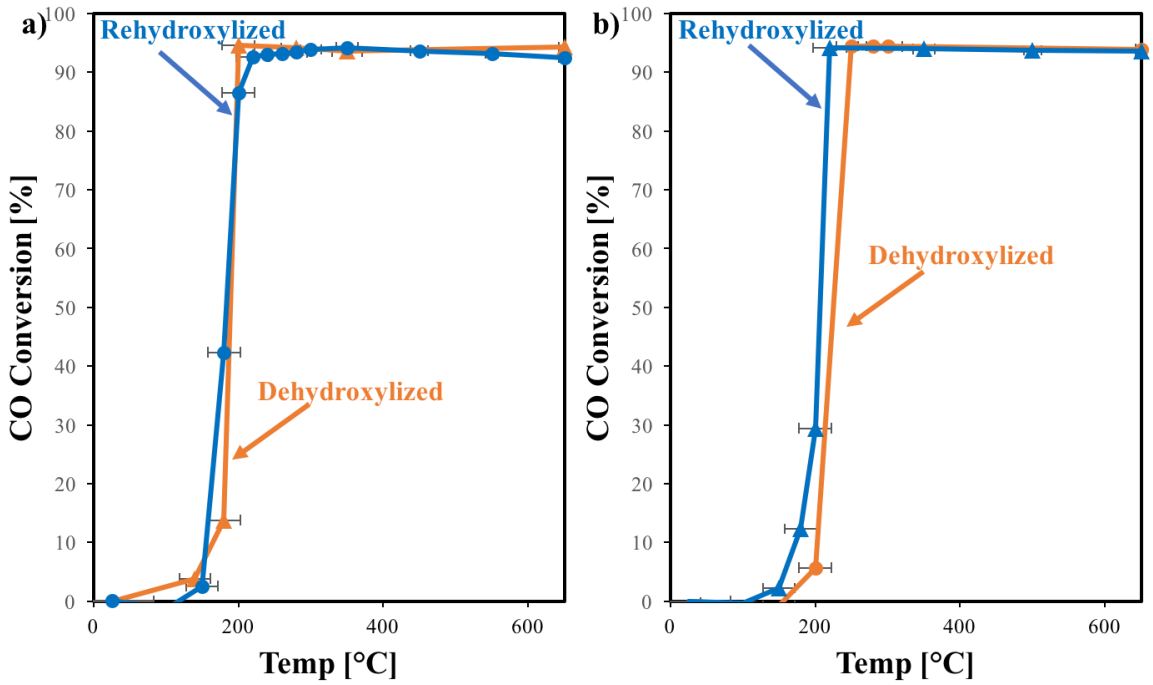

Figure 21 Temperature dependence of CO conversion on dehydroxylized catalysts (orange line) and rehydroxylized catalysts (blue line) of the 1st (a) and 3rd (b) reaction cycle.

Table 3 Summary of CO conversion, ignition temperature of catalysts for different reaction cycles.

Sample	Reaction Cycle	Max. Conversion [%]	Ignition Temperature* [ºC]
Pt @ rehydroxylized silica	1	96.17 ± 0.12	197.04
	2	94.59 ± 0.10	215.64
	3	94.06 ± 0.07	215.63

Table 3 (continued).

Pt @ dehydroxylized silica	1	96.10 ± 0.17	196.39
	2	96.36 ± 0.12	244.44
	3	95.48 ± 0.17	241.86

* Ignition temperature is calculated by linear regression at CO conversion overs 80%.

TEM images were taken before and after the reaction for both dehydroxylized and rehydroxylized catalysts and followed by particle size distribution analysis. From the average particle size, Pt NPs on both silica maintain around 1.6 nm before the reaction. However, the metal particles grow to 11.2 nm (shows as TEM images inside of the figure) for dehydroxylized silica with wide size distributions. Instead, the Pt NPs dispersed on rehydroxylized silica only grow to half of the former one, 5 nm.

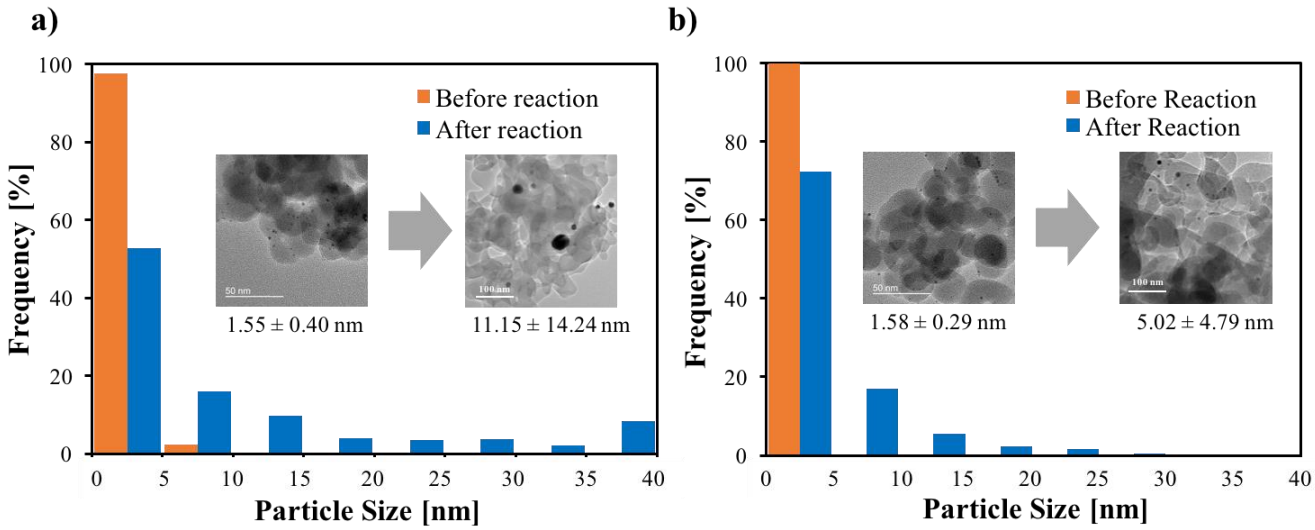

Figure 22 Particle size distribution analysis and TEM images of dehydroxylized catalysts (a) and rehydroxylized catalysts (b) before (orange) and after (blue) CO oxidation reaction.

In conclusion, the reactivity of rehydroxylized and dehydroxylized catalysts in CO oxidation confirms the catalysts with higher surface hydroxyl density are more stable through thermal treatment and reaction conditions because they sinter less and therefore loss less active sites compared to the dehydroxylized ones. The abnormal trend of extinction temperature higher than ignition temperature requires detailed studies. Ewing and co-workers modeled the net charge of Pt cluster dispersed on silica and found that the charge transfer from Pt to silica surface linearly relates with the number of Pt-O bonds.[62] The different charge transfer distribution due to divergent hydroxyl density on supported silica NPs could result in reactivity differences since the high density of electrons would have high reactivity. From the catalysts behavior shows as CO conversion in this study, there are limited differences between rehydroxylized catalysts with high silanol density and the ones with low density. They both achieve around 95 ~ 96% total conversion. How could electronic properties influence the catalytic activity and how big could this influence be in real catalysts are the two questions needed for further investigations.

4.0 CONCLUSION

Metal supported nanocatalysts attract considerable scientific attentions in recent year due to their large surface-to-volume ratios and low-coordinated active surface sites. Despite these extraordinary properties, the potential industrial use of high reactivity nanocatalysts is hindered by difficulties in thermal stability of these catalysts, which leads to high cost and low efficiency. Most of the small metal NPs dispersed on supports have excellent reaction performance when they are operated in mild experimental environment.

In this work, we synthesized small Pt NPs in 1~3 nm without added capping agents' protection, which enables Pt NPs directly to bond with surface of support, then dispersed Pt on amorphous silica with both fully hydroxylized and dehydroxylized, and characterized the surface hydroxyl groups combined TGA with BET. We proved that the surface silanol density can be easy tunable and linearly related with pretreatment temperature or calcination temperature. Salt recrystallization method used in synthesis of Pt on silica provided an efficient and effective way for separating highly stable NPs from solution.

Using these two different catalysts, we confirmed that the silica surface silanol number has directly relations with the Pt NPs thermal stability. The metal particles on rehydroxylized silica which has high silanol density grow to about half the size of the Pt NPs on dehydroxylized supports at high calcination temperature. Detailed discussion of average particle size obtained from TEM images and XRD size estimation are calculated and compared. Although from

volumetric average size achieved by Scherrer equation, Pt NPs dispersed on rehydroxylized silica even grown to 25 nm, further TEM demonstrated that over 80% of the particles still maintained small size through high thermal treatment. This is remarkably meaningful for catalysts in practice usage due to majority of small Pt NPs could still have high reactivity.

Furthermore, we studied the stability of the catalysts via testing reactivity in CO oxidation reaction. High temperature in operating CO oxidation led to a shift of the platinum particle size distribution towards larger diameters and loss of active sites on catalysts. This would in return deactivate catalysts, then cause decrease in reactivity. We found that the ignition temperature of rehydroxylized catalysts is 30 °C lower than the dehydroxylized ones through three reaction cycles, indicated that it was easier to ignite the catalysts with high hydroxyl density. The better performance of rehydroxylized catalysts were confirmed by observing under TEM before and after reaction. The Pt NPs dispersed on dehydroxylized silica sintered from 1.55 to 11.15 nm, while the rehydroxylized ones only grown from 1.58 to 5.02 nm.

Overall, our results confirm that the degree of surface hydroxylation of silica has strong impact on both stability and reactivity of the silica-supported metal nanocatalysts. Deep insights of experimental studies into the role of catalyst-support interactions on catalytic structure may serve to give an explicit direction of the design or optimization for future materials.

5.0 OUTLOOK

Metal NPs well dispersed on the surface of oxide supports such as silica, alumina, ceria from the majority of nanocatalysts with wide applications on sustainable energy, environmental pollution prevention, and biomedical fields. The catalytic activity, selectivity and lifetime of these materials always rely on metal particle size, detailed structure of support, and the surface chemistry of supports.

Previous modeling from our group developed a Pt clusters on amorphous silica model and concluded that the adhesive energy and net charge are linearly related with the number of Pt-silica bonds formed during the adsorption of Pt NPs on the silica surface [63] . The future work could base on these two tracks for an improved understanding of impact of metal-support interactions (Pt-silica bonds) on stability, reactivity, electronic properties, etc. of the catalysts.

5.1 IMPACT OF SURFACE INTERACTIONS ON ADHESIVE ENERGY

Campbell and coworkers suggested that sintering rate is directly related with the NP chemical potential regardless of sintering mechanisms.[58,59] Additionally, the chemical potential of metal NPs is directly related with adhesion energy. Since the metal-silica adhesive energy linearly relates with the Pt-silica bonds which can be tuned by amorphous silica hydroxyl density, there is a clear relation of sintering rate of metal NPs with the surface properties of the supports. This

work demonstrated that high silanol groups leads to increase in thermal stability through experiment techniques. Whether analyzing the particle average size grows with calcination temperature or testing the reactivity at high temperature condition, indirect methods are used to validate the relation of surface chemistry with the stability without any information of adhesive energy of metal-supports.

Nowadays, the energetics information between metal and support is limited due to the difficulty of measuring these energies.[109–111] Temperature programmed desorption (TPD) is widely used as measurements to obtain desorption energies (and thus adsorption energies).[109] However, this method cannot be used onto oxides supports since the metal particles would sinter while TPD ramping up temperature, which leads to unknown of exact surface structure. Hence, single crystal adsorption calorimetry (SCAC) was developed by King's group [112] and further modified by Campbell's group [113] to directly measure heats of adsorption of metal atoms, and introduced it to measure adhesion energies of metal films to single crystal supports. In this measurement, metal atoms are vaporized and deposit on a single crystal oxide thin film. Thus, the understanding of resulting metal single crystal film is required for further calculation. The average size and number density of supported metal nanoparticles which is crucial for determining adhesive energy [60] would change during this thin film grows. This information relies on a mathematical model to calculate the size and density of particles, based on low energy ion scattering spectroscopy (LEIS) data. Combined all these techniques, adhesive energy could be obtained from varies of metal on oxide supports. However, this process is quite tedious and time-consuming. In order to get accuracy results, investigated samples need to be carefully prepared into thin single crystal layer. All the equipment need to be calibrated within a small error deviation before the measurements.

To develop a novel technique to directly gather data of the adhesive energy of Pt with silica, we started a collaboration with Dr. Tevis Jacobs to first develop a measurement of adhesive energy by AFM (Atomic Force Microscopy). We observe the approaching process of Pt coated AFM probe with amorphous silica surface in the TEM (Transmission Electronic Microscopy). The probe will slowly approach the silica and stick on the surface due to attractive force at a specific distance. Combining this known distance, the cantilever spring force, and subtract the van der Waals, long-distance forces etc, the adhesive force can be obtained and compared. Figure 23 shows a schematic of experiment set up. This is the first time directly measuring the adhesive force and energy in an ambient environment and could be applied into different types of metal, supports to gather a comprehensive understanding of metal-support interactions at molecular level.

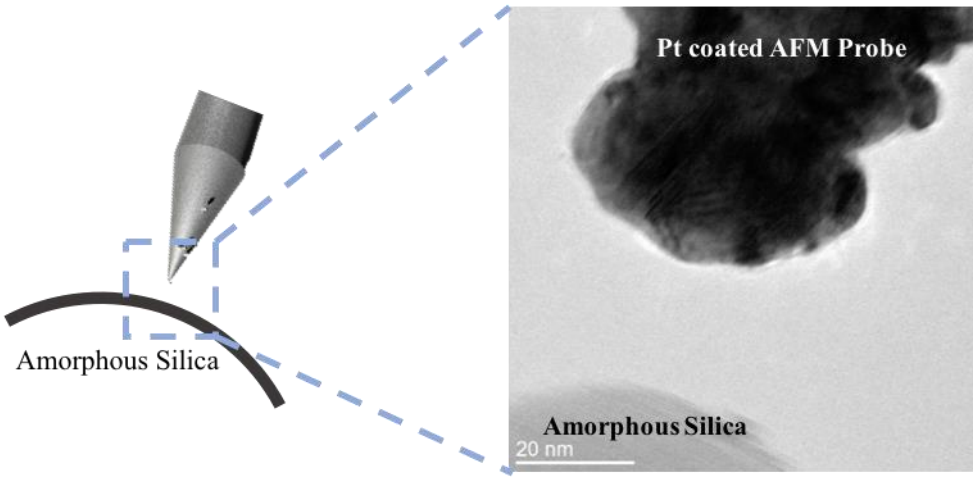

Figure 23 Schematic the process of the AFM probe contacts with silica surface.

5.2 IMPACT OF SURFACE INTERACTIONS ON NET CHARGE

Another field interested us is the net charge or electronic properties of the Pt cluster adsorbed on silica surface. Metal active sites surrounded by local electrons can dramatically impact the adsorbate binding. Overall, electron acceptors such as O_2, prone to bind with negatively charged sites. In contrast, positively charged sites are prefer binding with electron donors, like CO.[114] Ewing and co-workers modeled the net charge of Pt cluster on silica and found that the charge transfer from Pt to silica linearly related with the number of Pt-O bonds, net charge increased up to *2.4e* with five Pt-O bonds.[62] In addition, the positive charge located on the Pt atoms at the interface of metal and silica surface is remarkably high, which shows in Figure 24. The different charge transfer from metal to support could affect the catalytic activity has been proved by simulations.[115] Thus, the reactivity of silica-supported Pt nanocatalysts influenced by net charge distribution would be an enticing target for experimental measurements. For example, scanning tunneling spectroscopy (STS) could be used to obtain information of density of electrons as a function of sample energy. Wallis *et al.* studied the Pd atoms imbedded in Au atomic chains and characterized the predominant electronic features within the Au segments by STS and *dI/dV* imaging.[116] Besides, infrared spectroscopy (IR) vibration of CO stretch has reported to be sensitive to the surface charge and therefore could investigate the correlation of metal-silica bonds or coordinate number with electronic properties.[95]

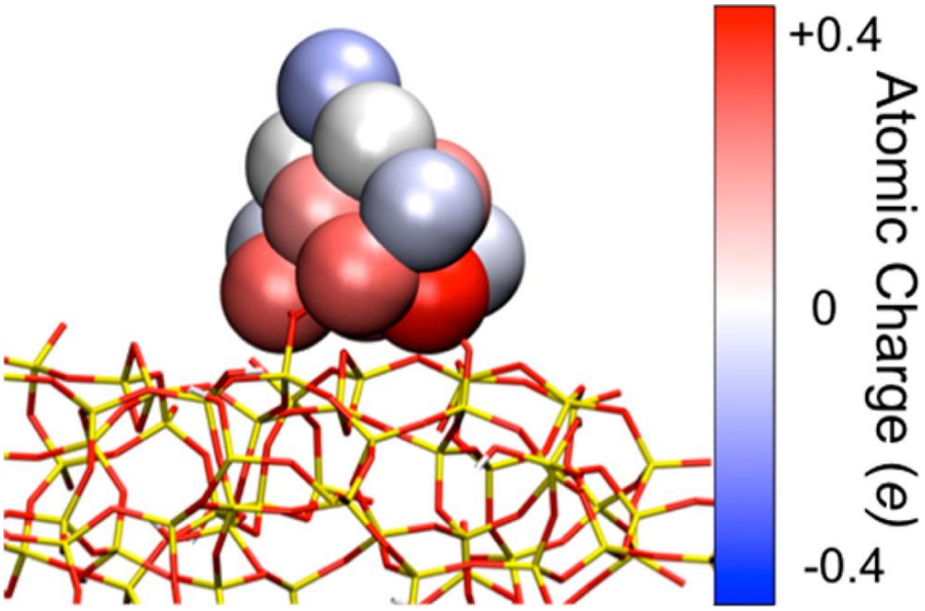

Figure 24 Distribution of charges on a supported Pt_{13} cluster with two Pt–O bonds. Atoms bonding to hydroxyls and their neighbors clearly undergo charge depletion, whereas low coordinated atoms not near the silica surface have slightly negative charges.[62]

APPENDIX A

CALCULATION OF CO OXIDATION

Carbon monoxide oxidation reaction would occur over platinum dispersed on amorphous silica surface, the system has following gas species: CO, O_2, CO_2 and Ar (inert gas), which the concentrations would be detected by the mass spectrometer at the outlet of the reactor. Hence the CO conversion can be calculated from the concentrations combined with gases base line obtained by bypassing the reactor and directly detected by MS.

$$CO + \frac{1}{2}O_2 \xrightarrow{Pt-Silica} CO_2$$

The CO conversion calculation is shown in the following.

$$X_{CO} = \frac{\dot{N}_{CO}^{in} - \dot{N}_{CO}^{out}}{\dot{N}_{CO}^{in}} \times 100\%$$

Where $\dot{N}_{CO}^{in}$ is the inlet CO flowrate, which is controlled by experiment condition. The outlet CO flowrate could be calculated by following equation:

$$\dot{N}_{CO}^{out} = y_{CO}^{out} \times \dot{N} = y_{CO}^{out} \times \frac{\dot{N}_{Ar}^{out}}{y_{Ar}^{out}} = y_{CO}^{out} \times \frac{\dot{N}_{Ar}^{in}}{y_{Ar}^{out}}$$

Flowrate of CO in outlet equals to its molar fraction y_{CO}^{out} times outlet total flowrate $\dot{N}$. Since we assume that the flowrate of inert gas (Ar) won't change before and after the reaction, we use its molar fraction y_{CO}^{out} and inlet flowrate $\dot{N}_{Ar}^{in}$ to calculate the outlet total flowrate $\dot{N}$. The molar fraction of each gas could be calculated directly through the signal intensity from MS and calibration data.

BIBLIOGRAPHY

1. Hemalatha, K. *et al.* Function of nanocatalyst in chemistry of organic compounds revolution: An overview. *J. Nanomater.* **2013,** 1–24 (2013).

2. Sinfelt, J. H. Catalysis: An old but continuing theme in chemistry. *Proc. Am. Philos. Soc.* **143,** 388–399 (1996).

3. Sinfelt, J. H. Some reflections on catalysis. *Chem. Ind.* 403–406 (1984).

4. Bylinsky, G. The magic of designer catalysts. *Fortune* **111,** 82 (1985).

5. Acmite Market Intelligence. *Global Catalyst Market*. *Market Report* (2015).

6. Catalysis. *Wikipedia* (2017). at <https://en.wikipedia.org/wiki/Catalysis>

7. Schwarz, J. A., Contescu, C. & Contescu, A. Methods for Preparation of Catalytic Materials. *Chem. Rev.* **95,** 477–510 (1995).

8. Munnik, P., De Jongh, P. E. & De Jong, K. P. Recent Developments in the Synthesis of Supported Catalysts. *Chem. Rev.* **115,** 6687–6718 (2015).

9. Wang, X., Feng, J., Bai, Y., Zhang, Q. & Yin, Y. Synthesis, Properties, and Applications of Hollow Micro-/Nanostructures. *Chem. Rev.* **116,** 10983–11060 (2016).

10. Gilroy, K. D., Ruditskiy, A., Peng, H. C., Qin, D. & Xia, Y. Bimetallic nanocrystals: Syntheses, properties, and applications. *Chem. Rev.* **116,** 10414–10472 (2016).

11. Kajbafvala, A. *et al.* Microwave-assisted synthesis of narcis-like zinc oxide nanostructures. *J. Alloys Compd.* **497,** 325–329 (2010).

12. Kajbafvala, A. *et al.* Nanostructure sword-like ZnO wires: Rapid synthesis and characterization through a microwave-assisted route. *J. Alloys Compd.* **469,** 293–297 (2009).

13. Lak, A. *et al.* Self-assembly of dandelion-like hydroxyapatite nanostructures via hydrothermal method. *J. Am. Ceram. Soc.* **91,** 3292–3297 (2008).

14. Zanganeh, S. *et al.* Self-assembly of boehmite nanopetals to form 3D high surface area nanoarchitectures. *Appl. Phys. A Mater. Sci. Process.* **99,** 317–321 (2010).

15. Zanganeh, S. *et al.* CVD fabrication of carbon nanotubes on electrodeposited flower-like Fe nanostructures. *J. Alloys Compd.* **507,** 494–497 (2010).

16. Mazloumi, M. *et al.* Boehmite nanopetals self assembled to form rosette-like nanostructures. *Mater. Lett.* **62,** 4184–4186 (2008).

17. Wettergren, K. *et al.* High sintering resistance of size-selected platinum cluster catalysts by suppressed ostwald ripening. *Nano Lett.* **14,** 5803–5809 (2014).

18. Dahl, S. *et al.* Role of Steps in N2 Activation on Ru(0001). *Phys. Rev. Lett.* **83,** 1814–1817 (1999).

19. Behrens, M. *et al.* The active site of methanol synthesis over Cu/ZnO/Al2O3 industrial catalysts. *Science (80-.).* **336,** 893–897 (2012).

20. Roduner, E. Size matters: why nanomaterials are different. *Chem. Soc. Rev.* **35,** 583 (2006).

21. Zhu, W. *et al.* Monodisperse Au nanoparticles for selective electrocatalytic reduction of CO2 to CO. *J. Am. Chem. Soc.* **135,** 16833–16836 (2013).

22. Bartholomew, C. H. & Farrauto, R. J. *Fundamentals of industrial catalytic process*. *Journal of Process Control* **5,** (John Wiley & Sons, 2005).

23. Sun, W. *et al.* High Surface Area Tunnels in Hexagonal WO $_3$. *Nano Lett.* **15,** 4834–4838 (2015).

24. Christesen, J. D., Pinion, C. W., Grumstrup, E. M., Papanikolas, J. M. & Cahoon, J. F. Synthetically encoding 10 nm morphology in silicon nanowires. *Nano Lett.* **13,** 6281–6286 (2013).

25. Kim, H. Y., Hybertsen, M. S. & Liu, P. Controlled Growth of Ceria Nanoarrays on Anatase Titania Powder: A Bottom-up Physical Picture. *Nano Lett.* **17,** 348–354 (2017).

26. Cushing, B. L., Kolesnichenko, V. L. & O'Connor, C. J. Recent advances in the liquid-phase syntheses of inorganic nanoparticles. *Chem. Rev.* **104,** 3893–3946 (2004).

27. Semagina, N. & Kiwi-Minsker, L. Recent Advances in the Liquid-Phase Synthesis of Metal Nanostructures with Controlled Shape and Size for Catalysis. *Catal. Rev.* **51,** 147–217 (2009).

28. Curtis, A. C. *et al.* Preparation and structural characterization of an unprotected copper sol. *J. Phys. Chem.* **92,** 2270–2275 (1988).

29. Cardenas-Trivino, G., Klabunde, K. J. & Dale, E. B. Living colloidal palladium in nonaqueous solvents. Formation, stability, and film-forming properties. Clustering of metal atoms in organic media. 14. *Langmuir* **3,** 986–992 (1987).

30. Tano, T., Esumi, K. & Meguro, K. Preparation of organopalladium sols by thermal decomposition of palladium acetate. *J. Colloid Interface Sci.* **133,** 530–533 (1989).

31. Wang, Y., Ren, J., Deng, K., Gui, L. & Tang, Y. Preparation of tractable platinum, rhodium, and ruthenium nanoclusters with small particle size in organic media. *Chem. Mater.* **12,** 1622–1627 (2000).

32. Ek, S., Root, A., Peussa, M. & Niinistö, L. Determination of the hydroxyl group content in silica by thermogravimetry and a comparison with 1H MAS NMR results. *Thermochim. Acta* **379,** 201–212 (2001).

33. Hofmann, U., Endell, K. & Wilm, D. Röntgenographische und kolloidchemische Untersuchungen über Ton. *Angew. Chemie* **47,** 539–547 (1934).

34. Rideal, E. K. Introductory address. *Trans. Faraday Soc.* **32,** 3 (1936).

35. Carman, P. C. Constitution of colloidal silica. *Trans. Faraday Soc.* **36,** 964–973 (1940).

36. Zhuravlev, L. T. The surface chemistry of amorphous silica. *Colloids Surfaces A Physicochem. Eng. Asp.* **173,** 1–38 (2000).

37. Iler, R. K. *The chemistry of silica: solubility, polymerization, colloid and surface properties, and biochemistry*. *Lavoisierfr* (Wiley, 1979). doi:10.1002/ange.19800920433

38. Elliott, J. a. Novel approaches to multiscale modelling in materials science. *Int. Mater. Rev.* **56,** 207–225 (2011).

39. Zhuravlev, L. T. The surface chemistry of amorphous silica . Zhuravlev model. *Colloids Surfaces A Physicochem. Eng. Asp.* **173,** 1–38 (2000).

40. Haruta, M. Catalysis of gold nanoparticles deposited on metal oxides. *Cattech* **6,** 102–115 (2002).

41. Wolf, A. & Schüth, F. A systematic study of the synthesis conditions for the preparation of highly active gold catalysts. *Appl. Catal. A Gen.* **226,** 1–13 (2002).

42. Liu, P. & Rodriguez, J. A. Water-gas-shift reaction on metal nanoparticles and surfaces. *J. Chem. Phys.* **126,** 164705 (2007).

43. Deluga, G. a, Salge, J. R., Schmidt, L. D. & Verykios, X. E. Renewable hydrogen from ethanol by autothermal reforming. *Science* **303,** 993–997 (2004).

44. Chang, T. C., Chen, J. J. & Yeh, C. T. Temperature-programmed reduction and temperature-resolved sorption studies of strong metal-support interaction in supported palladium catalysts. *J. Catal.* **96,** 51–57 (1985).

45. Pretorius, R., Harris, J. M. & Nicolet, M. A. Reaction of thin metal films with SiO2 substrates. *Solid State Electron.* **21,** 667–675 (1978).

46. Chen, M. & Schmidt, L. D. Morphology and sintering of Pt crystallites on amorphous SiO2. *J. Catal.* **55,** 348–360 (1978).

47. Xu, X., He, J.-W. & Wayne Goodman, D. A surface spectroscopic study of metal-support interactions: model studies of copper on thin SiO2 films. *Surf. Sci.* **284,** 103–108 (1993).

48. Xu, X. & Goodman, D. W. Metal deposition onto oxides: An unusual low initial sticking probability for copper on SiO2. *Appl. Phys. Lett.* **61,** 1799–1801 (1992).

49. Xu, X., Szanyi, J., Xu, Q. & Goodman, D. W. Structural and catalytic properties of model silica- supported palladium catalysts: a comparison to single crystal surfaces. *Catal. Today* **21,** 57–69 (1994).

50. Powell, B. R. & Whittington, S. E. Encapsulation: A new mechanism of catalyst deactivation. *J. Catal.* **81,** 382–393 (1983).

51. Oetelaar, L. C. A. Van Den, Partridge, A., Stapel, P. J. A., Flipse, C. F. J. & Brongersma, H. H. A Surface Science Study of Model Catalysts . 1 . Quantitative Surface Analysis of Wet-Chemically Prepared Cu / SiO 2 Model Catalysts. *J. Phys. Chem. B* 9532–9540 (1998). doi:10.1021/jp9829997

52. Mayer, J. T., Lin, R. F. & Garfunkel, E. Surface and bulk diffusion of adsorbed nickel on ultrathin thermally grown silicon dioxide. *Surf. Sci.* **265,** 102–110 (1992).

53. Zhou, J. B., Gustafsson, T., Lin, R. F. & Garfunkel, E. Medium energy ion scattering study of Ni on ultrathin films of SiO2 on Si(111). *Surf. Sci.* **284,** 67–76 (1993).

54. Van, D. O. L. C. a, Van, D. O. R. J. a, Partridge, a, Flipse, C. F. J. & Brongersma, H. H. Reaction of nanometer-sized Cu particles with a SiO2 substrate. *Appl. Phys. Lett.* **74,** 2954–2956 (1999).

55. Min, B. K., Santra, A. K. & Goodman, D. W. Understanding silica-supported metal catalysts: Pd/silica as a case study. *Catal. Today* **85,** 113–124 (2003).

56. Sheu, L. L., Karpinski, Z. & Sachtler, W. M. H. Effects of palladium particle size and palladium silicide formation on Fourier transform infrared spectra and carbon monoxide adsorbed on palladium/silicon dioxide catalysts . *J. Phys. Chem.* **93(12),** 4890 (1989).

57. Juszczyk, W. & Karpiński, Z. Characterization of Supported Palladium Catalysts II. Pd/SiO2. *J. Catal.* **117,** 519–532 (1989).

58. Campbell, C. T. & Sellers, J. R. V. Anchored metal nanoparticles: Effects of support and size on their energy, sintering resistance and reactivity. *Faraday Discuss.* **162,** 9 (2013).

59. Campbell, C. T. The energetics of supported metal nanoparticles: Relationships to sintering rates and catalytic activity. *Acc. Chem. Res.* **46,** 1712–1719 (2013).

60. Farmer, J. A. & Campbell, C. T. Ceria Maintains Smaller Metal Catalyst Particles by Strong Metal-Support Bonding. *Science (80-.).* **329,** 933–936 (2010).

61. Hemmingson, S. L. & Campbell, C. T. Trends in Adhesion Energies of Metal Nanoparticles on Oxide Surfaces: Understanding Support Effects in Catalysis and Nanotechnology. *ACS Nano* acsnano.6b07502 (2016). doi:10.1021/acsnano.6b07502

62. Ewing, C. S. *et al.* Structural and Electronic Properties of Pt13 Nanoclusters on Amorphous Silica Supports. *J. Phys. Chem. C* 2503–2512 (2015). doi:10.1021/jp5105104

63. Ewing, C. S., Veser, G., McCarthy, J. J., Johnson, J. K. & Lambrecht, D. S. Effect of Support Preparation and Nanoparticle Size on Catalyst-Support Interactions between Pt and Amorphous Silica. *J. Phys. Chem. C* (2015). doi:10.1021/acs.jpcc.5b05763

64. Werner Stober, A. F. Controlled Growth of Monodisperse Silica Spheres in the Micron Size Range 1. *J. Colliod Interface Sci.* **26,** 62–69 (1968).

65. Wang, J. *et al.* Two-phase synthesis of monodisperse silica nanospheres with amines or ammonia catalyst and their controlled self-assembly. *ACS Appl. Mater. Interfaces* **3,** 1538–1544 (2011).

66. Ewing, C. S., Bhavsar, S., Veser, G., McCarthy, J. J. & Johnson, J. K. Accurate amorphous silica surface models from first-principles thermodynamics of surface dehydroxylation. *Langmuir* **30,** 5133–41 (2014).

67. Ewing, C. S., Veser, G., McCarthy, J. J., Johnson, J. K. & Lambrecht, D. S. Effect of Support Preparation and Nanoparticle Size on Catalyst-Support Interactions between Pt and Amorphous Silica. *J. Phys. Chem. C, Submitt.* (2015). doi:10.1021/acs.jpcc.5b05763

68. Yuan Wang, Jiawen Ren, K. D. et al. Preparation of Tractable Platinum, Rhodium, and Ruthenium Nanoclusters with Small Particle Size in Organic Media. *Chem. Mater.* **12,** 1622–1627 (2000).

69. Scherrer, P. Göttinger Nachrichten Math. *Phys* **2,** 98–100 (1918).

70. Patterson, A. L. The scherrer formula for X-ray particle size determination. *Phys. Rev.* **56,** 978–982 (1939).

71. Ismail, I. M. K. Cross-Sectional Areas of Adsorbed N2, Ar, Kr, and O2 on Carbons and Fumed Silicas at Liquid-Nitrogen Temperature. *Langmuir* **8,** 360–365 (1992).

72. Schrader, I. *et al.* Surface Chemistry of ‘unprotected’ Nanoparticles: A Spectroscopic Investigation on Colloidal Particles. *J. Phys. Chem. C* **119,** 17655–17661 (2015).

73. Bock, C., Paquet, C., Couillard, M., Botton, G. A. & MacDougall, B. R. Size-selected synthesis of PtRu nano-catalysts: Reaction and size control mechanism. *J. Am. Chem. Soc.* **126,** 8028–8037 (2004).

74. Yang, J., Deivaraj, T. C., Too, H. P. & Lee, J. Y. Acetate stabilization of metal nanoparticles and its role in the preparation of metal nanoparticles in ethylene glycol. *Langmuir* **20,** 4241–4245 (2004).

75. Kiselev, A. V & Dreving, V. P. Experimental Methods in Adsorption and Molecular Chromatography. *Moscow State Univ* (1973).

76. Zhuravlev, L. T. CHARACTERIZATION OF AMORPHOUS SILICA SURFACE. *React. Kinet. Catal. Lett.* **50,** 15–25 (1993).

77. Zhuravlev, L. T. Concentration of Hydroxyl Groups on the Surface of Amorphous Silicas. *Langmuir* 316–318 (1987).

78. Potapov, V. V. & Zhuravlev, L. T. Temperature dependence of the concentration of silanol groups in silica precipitated from a hydrothermal solution. *Glas. Phys. Chem.* **31,** 661–670 (2005).

79. Zhuravlev, L. T. & Potapov, V. V. Density of silanol groups on the surface of silica precipitated from a hydrothermal solution. *Russ. J. Phys. Chem.* **80,** 1119–1128 (2006).

80. Yuasa, S., Okabayashi, M., Ohno, H., Suzuki, K. & Kusumoto, K. Amorphous, spherical inorganic compound and process for preparation thereof. (1988). at <https://www.google.com/patents/US4764497>

81. Kang, S. *et al.* Preparation and characterization of epoxy composites filled with functionalized nanosilica particles obtained via sol–gel process. *Polymer (Guildf).* **42,** 879–887 (2001).

82. Zhuravlev, L. T. Surface characterization of amorphous of work from the former USSR. *Colloids Surfaces A Physicochem. Eng. Asp.* **74,** 71–90 (1993).

83. Mueller, R., Kammler, H. K., Wegner, K. & Pratsinis, S. E. OH surface density of SiO2 and TiO2 by thermogravimetric analysis. *Langmuir* **19,** 160–165 (2003).

84. R. F. De Farias, C. A. Thermogravimetry as a reliable tool to estimate the density of silanols on a silica gel surface.pdf. *J. Therm. Anal.* **53,** 751–756 (1998).

85. Mrowiec-Bialo, J. Determination of hydroxyls density in the silica-mesostructured cellular foams by thermogravimetry. *Thermochim. Acta* **443,** 49–52 (2006).

86. Zhuravlev, L. T. The surface chemistry of amorphous silica. Zhuravlev model. *Colloids Surfaces A Physicochem. Eng. Asp.* **173,** 1–38 (2000).

87. Gorelik, R. L. *et al.* Investigation into the Mechanism of Formation of Utraporosity in Silica Gels during Hydrothermal Treatment. *Kolloidn. Zh* **33,** 51–58 (1971).

88. Stone, P., Poulston, S., Bennett, R. A. & Bowker, M. Scanning tunnelling microscopy investigation of sintering in a model supported catalyst: nanoscale Pd on TiO2(110). *Chem. Commun.* **2,** 1369–1370 (1998).

89. Baker, R. T. K., Harris, P. S. & Thomas, R. B. Direct observation of particle mobility on a surface in a gaseous environment. *Surf. Sci.* **46,** 311–316 (1974).

90. Smilgies, D. M. Scherrer grain-size analysis adapted to grazing-incidence scattering with area detectors. *J. Appl. Crystallogr.* **42,** 1030–1034 (2009).

91. Sehested, J. Sintering of nickel steam-reforming catalysts. *J. Catal.* **217,** 417–426 (2003).

92. Szwarc, R., Plante, E. R. & Diamond, J. J. Vapor pressure and heat of sublimation of tungsten. *J. Res. Natl. Bur. Stand. Sect. A Phys. Chem.* **69A,** 417 (1965).

93. Borchert, H. *et al.* Determination of nanocrystal sizes: A comparison of TEM, SAXS, and XRD studies of highly monodisperse CoPt 3 particles. *Langmuir* **21,** 1931–1936 (2005).

94. Morrow, B. a & Cody, I. a. Infrared studies of reactions on oxide surfaces. 5. Lewis acid sites on dehydroxylated silica. *J. Phys. Chem.* **80,** 1995–1998 (1976).

95. Rodriguez, a, Truong, C. M. & Goodmanb, D. W. Infrared vibrational surfaces studies of CO adsorption on Cu / Pt (lll) and CuPt (111). *J.Chem.Phys* **96,** 7814–7825 (1992).

96. Paul J. Berlowitz, Charles H. F. Peden, and D. W. G. S. Kinetics of CO Oxidation on Single-Crystal Pd, Pt, and Ir. *J. Phys. Chem.* **92,** 5213–5221 (1988).

97. Goodman, D. W. Model Studies in Catalysis Using Surface Science Probes. *Chem. Rev.* **95,** 523–536 (1995).

98. Rodriguez, J. A. & Wayne Goodman, D. High-pressure catalytic reactions over single-crystal metal surfaces. *Surf. Sci. Rep.* **14,** 1–107 (1991).

99. Somorjai, G. A. & McCrea, K. R. in *Advances in Catalysis* **45,** 385–438 (2000).

100. Völkening, S. & Wintterlin, J. CO oxidation on Pt(111)-scanning tunneling microscopy experiments and Monte Carlo simulations. *J. Chem. Phys.* **114,** 6382–6395 (2001).

101. Chen, M. S. The Structure of Catalytically Active Gold on Titania. *Science (80-.).* **306,** 252–255 (2004).

102. Hong, S. & Richardson, H. H. Infrared reflection-absorption spectroscopy of adsorbates on a platinum (100) surface during carbon monoxide oxidation. *J. Phys. Chem.* **97,** 1258–1261 (1993).

103. Vlachos, D. G. & Bui, P. A. Catalytic ignition and extinction of hydrogen: Comparison of simulations and experiments. *Surf. Sci.* **364,** L625–L630 (1996).

104. Rinnemo, M. *et al.* Catalytic ignition in the CO-O2 reaction on platinum: Experiment and simulations. *Surf. Sci.* **376,** 297–309 (1997).

105. Mhadeshwar, A. B. & Vlachos, D. G. A thermodynamically consistent surface reaction mechanism for CO oxidation on Pt. *Combust. Flame* **142,** 289–298 (2005).

106. McCrea, K. R., Parker, J. S. & Somorjai, G. A. The role of carbon deposition from CO dissociation on platinum crystal surfaces during catalytic CO oxidation: Effects on turnover rate, ignition temperature, and vibrational spectra. *J. Phys. Chem. B* **106,** 10854–10863 (2002).

107. Yang, J. Effect of sintering on the catalytic activity of a Pt based catalyst for CO oxidation: Experiments and modeling. *Appl. Catal. B Environ.* **83,** 229–239 (2008).

108. Subbotin, A. N., Gudkov, B. S., Dykh, Z. L. & Yakerson, V. I. Temperature hysteresis in CO oxidation on catalysts of various nature. *React. Kinet. Catal. Lett.* **66,** 97–104 (1999).

109. Campbell, C. T. & Starr, D. E. Metal adsorption and adhesion energies on MgO(100). *J. Am. Chem. Soc.* **124,** 9212–9218 (2002).

110. Sharp, J. C., Yao, Y. X. & Campbell, C. T. Silver nanoparticles on Fe3O4(111): Energetics by Ag adsorption calorimetry and structure by surface spectroscopies. *J. Phys. Chem. C* **117,** 24932–24936 (2013).

111. Farmer, J. A., Baricuatro, J. H. & Campbell, C. T. Ag adsorption on reduced CeO2(111) thin films. *J. Phys. Chem. C* **114,** 17166–17172 (2010).

112. Borroni-Bird, C. E. & King, D. A. An ultrahigh vacuum single crystal adsorption microcalorimeter. *Rev. Sci. Instrum.* **62,** 2177–2185 (1991).

113. Stuckless, J. T., Frei, N. A. & Campbell, C. T. A novel single-crystal adsorption calorimeter and additions for determining metal adsorption and adhesion energies. *Rev. Sci. Instrum.* **69,** 2427–2438 (1998).

114. Wallace, W. T. & Whetten, R. L. Carbon monoxide adsorption on selected gold clusters: Highly size-dependent activity and saturation compositions. *J. Phys. Chem. B* **104,** 10964–10968 (2000).

115. Stamatakis, M., Christiansen, M. A., Vlachos, D. G. & Mpourmpakis, G. Multiscale modeling reveals poisoning mechanisms of MgO-supported Au clusters in CO oxidation. *Nano Lett.* **12,** 3621–3626 (2012).

116. Wallis, T. M., Nilius, N., Mikaelian, G. & Ho, W. Electronic properties of artificial Au chains with individual Pd impurities. *J. Chem. Phys.* **122,** (2005).

117. Howard W. Turner, Anthony F. Volpe Jr. & W.H. Weinberg. High-throughput heterogeneous catalyst research. *Surf. Sci.* **603,** 1763–1769 (2009).